THE ASTROPHYSICAL JOURNAL, 515:842–867, 1999 April 20
© 1999. The American Astronomical Society. All rights reserved. Printed in U.S.A.

THREE-DIMENSIONAL STEREOSCOPIC ANALYSIS OF SOLAR ACTIVE REGION LOOPS. I. *SOHO*/EIT OBSERVATIONS AT TEMPERATURES OF (1.0–1.5) × 10^6 K

MARKUS J. ASCHWANDEN[1]
Department of Astronomy, University of Maryland, College Park, MD 20742; markus@astro.umd.edu
JEFFREY S. NEWMARK
Space Applications Corporation, Vienna, VA 22180
JEAN-PIERRE DELABOUDINIÈRE
Institute d'Astrophysique Spatiale, Université Paris XI, 91405 Orsay Cedex, France
WERNER M. NEUPERT
Hughes SXT Corporation, Lanham, MD 20706
J. A. KLIMCHUK
Space Science Division, Code 7675, Naval Research Laboratory, Washington, DC 20375-5352
G. ALLEN GARY
ES82-Solar Physics Branch, Space Science Laboratory, NASA/MSFC, Huntsville, AL 35812
FABRICE PORTIER-FOZZANI
Laboratoire d'Astronomie Spatiale, CNRS, BP 8, 13376 Marseille Cedex 12, France
AND
ARIK ZUCKER
ETH, Institute Astronomy, Häldeliweg 15, CH-8092 Zurich, Switzerland
Received 1998 May 13; accepted 1998 November 23

ABSTRACT

The three-dimensional structure of solar active region NOAA 7986 observed on 1996 August 30 with the Extreme-Ultraviolet Imaging Telescope (EIT) on board the *Solar and Heliospheric Observatory* (*SOHO*) is analyzed. We develop a new method of *dynamic stereoscopy* to reconstruct the three-dimensional geometry of dynamically changing loops, which allows us to determine the orientation of the mean loop plane with respect to the line of sight, a prerequisite to correct properly for projection effects in three-dimensional loop models. With this method and the filter-ratio technique applied to EIT 171 and 195 Å images we determine the three-dimensional coordinates $[x(s), y(s), z(s)]$, the loop width $w(s)$, the electron density $n_e(s)$, and the electron temperature $T_e(s)$ as a function of the loop length s for 30 loop segments. Fitting the loop densities with an exponential density model $n_e(h)$ we find that the mean of inferred scale height temperatures, $T_e^{\lambda} = 1.22 \pm 0.23$ MK, matches closely that of EIT filter-ratio temperatures, $T_e^{\rm EIT} = 1.21 \pm 0.06$ MK. We conclude that these cool and rather large-scale loops (with heights of $h \approx 30$–225 Mm) are in hydrostatic equilibrium. Most of the loops show no significant thickness variation $w(s)$, but we measure for most of them a positive temperature gradient ($dT/ds > 0$) across the first scale height above the footpoint. Based on these temperature gradients we find that the conductive loss rate is about 2 orders of magnitude smaller than the radiative loss rate, which is in strong contrast to hot active region loops seen in soft X-rays. We infer a mean radiative loss time of $\tau_{\rm rad} \approx 40$ minutes at the loop base. Because thermal conduction is negligible in these cool EUV loops, they are *not in steady state*, and radiative loss has entirely to be balanced by the heating function. A statistical heating model with recurrent heating events distributed along the entire loop can explain the observed temperature gradients if the mean recurrence time is $\lesssim 10$ minutes. We computed also a potential field model (from *SOHO*/MDI magnetograms) and found a reasonable match with the traced EIT loops. With the magnetic field model we determined also the height dependence of the magnetic field $B(h)$, the plasma parameter $\beta(h)$, and the Alfvén velocity $v_{\rm A}(h)$. No correlation was found between the heating rate requirement E_{H0} and the magnetic field $B_{\rm foot}$ at the loop footpoints.

Subject headings: Sun: activity — Sun: corona — Sun: UV radiation — techniques: image processing

1. INTRODUCTION

The evolution of coronal plasma loops, beginning from the well-kept secret of the elusive heating mechanism, to the somewhat better understood conductive and radiative cooling processes, and the various transitions from steady state to nonequilibrium states, still represents a key problem of coronal plasma physics. Because the average temperature of the solar corona ranges around $T_e \approx 1.5$ MK, this temperature seems to reflect the most likely steady state condition of coronal structures, demarcating at the same time a watershed where cooling and heating processes start to lose equilibrium. It is therefore a physically meaningful choice to distinguish between *cool*[2] and *hot* loops

[1] Current address: Lockheed-Martin ATC, Solar and Astrophysics Laboratory, Department H1-12, Building 252, 3251 Hanover Street, Palo Alto, CA 94304; aschwanden@sag.lmsal.com.

[2] The temperature range of $T_e \lesssim 1.5$ MK that we denote as *cool* here is sometimes also termed *intermediate* temperatures (e.g., Brown 1996), whereas loops with temperatures of $T_e \lesssim 10^5$ K are referred to as *cool* loops (e.g., Martens & Kuin 1982).

with respect to this *maximum likelihood temperature* $T_e \approx$ 1.5 MK, which also separates roughly the line-formation temperatures in the EUV/XUV and soft X-ray (SXR) wavelength regimes. Coronal loops in EUV/XUV wavelengths could only be studied with few instruments, mainly from the spacecraft missions *Skylab*, *SOHO*, *Transition Region And Coronal Explorer* (*TRACE*), and from a few short-duration rocket flights (e.g., American Science and Engineering [AS&E], High-Resolution Telescope and Spectrograph [HRTS], or Solar EUV Rocket Telescope and Spectrograph [SERTS]). The scarce EUV observations before the launch of *SOHO* provided little systematic information on the physical structure of cooler active region loops in the temperature regime of $T_e \lesssim 1.5$ MK, as opposed to the much more frequently studied hotter loops ($T_e \gtrsim 1.5$ MK) in SXR (with *OSO 8*, *P78-1*, *Hinotori*, *SMM*/XRP, *Yohkoh*/SXT, *Coronas*, etc.). A number of statistical studies exist on hot active region loops observed in SXRs (e.g., Pallavicini, Serio, & Vaiana 1977; Rosner, Tucker, & Vaiana 1978; Cheng 1980; Porter & Klimchuk 1995; Klimchuk & Gary 1995; Kano & Tsuneta 1995, 1996), but there are no comparable statistics available on cooler active region loops observed at temperatures of $T_e = 1.0$–1.5 MK in EUV. Moreover, not much effort has been invested in the three-dimensional reconstruction of coronal loops at any wavelength so far (although the technology is ready; see, e.g., Gary 1997). This work represents a first comprehensive statistical study on physical parameters of *cool* active region loops in the $T_e = 1.0$–1.5 MK temperature range, measured with unprecedented accuracy using a newly developed three-dimensional reconstruction method called *dynamic stereoscopy*.

Let us quickly review some highlights of earlier work on EUV loops in the $T_e \approx 1.0$–1.5 MK temperature range. A comprehensive account on literature before 1991 can be found in Bray et al. (1991). The *Skylab* XUV spectroheliograph provided images with 2″–3″ resolution at wavelengths of 180–630 Å, including the Mg IX line with a formation temperature of $T_e = 0.9$ MK. Dere (1982) analyzed such XUV loops and found (1) that they are close to hydrostatic equilibrium (within the uncertainties of the unknown three-dimensional geometry) and (2) that hot ($T_e > 1$ MK) loops do not have a cool core structure as suggested by Foukal (1975). Sheeley (1980) studied the temporal variability of EUV loops and found lifetimes of ≈ 1.5 hr for 1 MK loops, somewhat longer than those of 0.5 MK loops. This lifetime of 1 MK loops, estimated by Sheeley from time-lapse movies, is actually close to the value we infer for the radiative cooling time from *SOHO*/EIT data. Observations with SERTS revealed that the brightest structures seen in Mg IX are not spatially coincident with hotter coronal loops seen in SXR but are rooted in chromospheric He II features and thus seem to trace out cooler coronal loops with apex temperatures of $T_e \lesssim 1$ MK (Brosius et al. 1997). The existence of numerous cooler loops has also been postulated from the observed discrepancy between SXR-inferred temperatures of active regions and simultaneous radio brightness temperature measurements because the former include only the contributions from hot loops, whereas the latter are sensitive to the combined free-free opacity of both hot and cool loops (Webb et al. 1987; Nitta et al. 1991; Schmelz et al. 1992, 1994; Brosius et al. 1992; Klimchuk & Gary 1995; Vourlidas & Bastian 1996). The most recent work on EUV loops comes from *SOHO*/EIT (Neupert et al. 1998; Aschwanden et al. 1998a, 1998b) and *SOHO*/CDS (Fludra et al. 1997; Brekke et al. 1997). Neupert et al. (1998) analyzed a long-lived loop structure and an open-field radial feature and found (1) that they are close to hydrostatic equilibrium (within the uncertainties of the unknown three-dimensional geometry), and (2) that radiative energy loss strongly dominates conductive energy loss at these loop temperatures of $T_e = 1.0$–1.5 MK, requiring a heating function that scales with the squared density, $E_H \propto n_e^2$. The temporal variability and lifetime of EUV loops can now best be studied from *SOHO*/EIT movies (Newmark et al. 1997).

What progress can we expect from a new analysis of active region loops, using the most recent EUV data available from *SOHO*/EIT? To accomplish sensible tests of theoretical models on heating and cooling processes, accurate physical parameters from *resolved single loops* are needed. However, most of the previous literature deals with line-of-sight averaged quantities without discriminating between single loops. For a proper determination of physical parameters from single active region loops, a number of analysis problems have to be overcome.

1. Geometric loop definition
2. Identification and tracing of loops in images
3. Disentangling of nested loops
4. Separation of overlying or closely spaced loops
5. Discrimination of multiple loops along the line of sight
6. Three-dimensional reconstruction of loop geometry and deprojection
7. Temperature discrimination along the line of sight
8. Reliable temperature and emission measure determination.

Most of these problems have not been treated in a systematic way in previous studies. Here we present the results of a new approach, making use of the principle of dynamic stereoscopy to reconstruct the three-dimensional orientation of loops, which provides a reliable method to obtain more accurate physical parameters as a function of the loop length, properly corrected for line-of-sight related projection effects. The enhanced accuracy is expected to allow for more rigorous tests of theoretical loop models.

In § 2 we describe the stereoscopic data analysis of 30 loops observed with *SOHO*/EIT at a wavelength band centered around Fe IX, Fe X at 171 Å. In § 3 we apply physical loop models to the data and investigate loop scaling laws. A summary and conclusions are given in § 4.

2. STEREOSCOPIC DATA ANALYSIS

2.1. *Data Set*

The investigated active region is a long-lived coronal structure that was present during several solar rotations, from its apparition in 1996 July until its disappearance in 1996 September (Hudson et al. 1998; Harvey & Hudson 1998), numbered as NOAA 7978, 7981, 7986 during consecutive rotations. We concentrate here on the central meridian transit on 1996 August 30, when the dipolar magnetic field structure offered the most favorable perspective to disentangle the "jungle" of nested loops.

An Fe IX/Fe X image recorded with *SOHO*/EIT (Delaboudinière et al. 1995) at a wavelength of 171 Å on 1996 August 30, 0020:14 UT is shown in Figure 1 (*top*). For stereoscopic correlations we will also use EIT images from

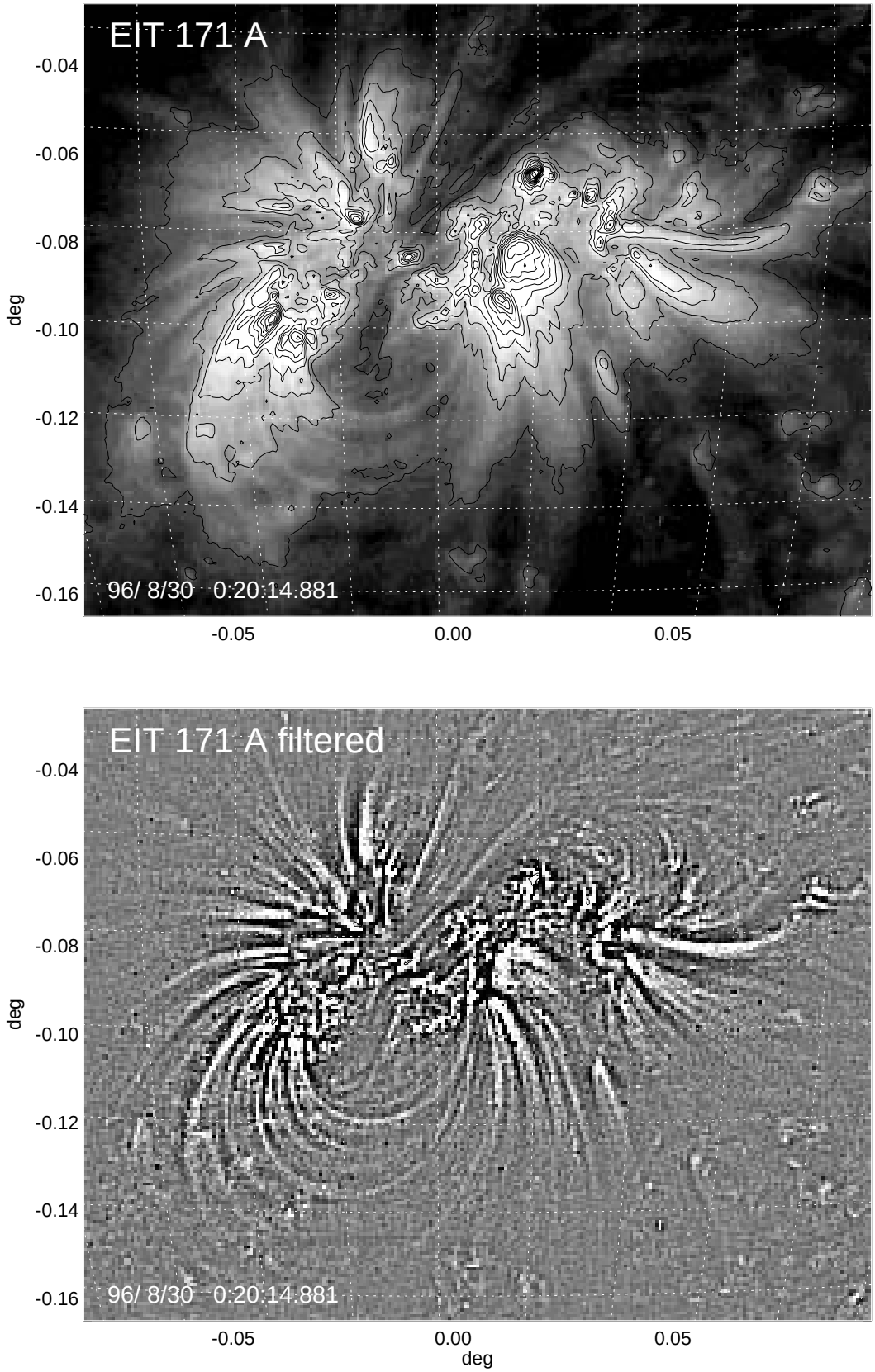

FIG. 1.—*SOHO*/EIT Fe IX/Fe X image of active region AR 7986, recorded on 1996 August 30, 0020:14 UT, at a wavelength of 171 Å, sensitive in the temperature range of $T_e = 1.0$–1.5 MK (*top*). The gray scales of the image is scaled logarithmically in flux, the contours correspond to increments of 100 DN (data numbers). The heliographic grid has a spacing of 5°. The filtered image (*bottom*) was created by subtracting a smoothed image (using a boxcar of 3×3 pixels) from the original image, in order to enhance the loop fine structure.

the previous (1996 August 29, 0015:15 UT) and following day (1996 August 31, 0010:14 UT). The multiloop structure of this active region is clearly visible in the high-pass filtered rendering shown in Figure 1 (*bottom*). The filtered image is simply created by subtracting a smoothed image (with a boxcar average over 3×3 pixels) from the original image. The original (full disk) image has a pixel size of 2″.616 and was recorded with an exposure time of 3.5 s. The absolute coordinate system of the full-disk image was established by fitting a circle to the solar limb (at 30 limb positions). The accuracy of the so-defined Sun center position is estimated to be $\sigma_x \approx 1$ pixel/$30^{1/2} \approx 0.2$ pixel. The offset of the Sun center position (x_0', y_0') provided (by an automatic limb-fitting routine) in the FITS header of the archive EIT image with respect to our value (x_0, y_0) is found to be $(x_0' - x_0) = +0.5$ and $(y_0' - y_0) = -3.9$ pixels. For the solar radius we find a difference of $(r_0' - r_0) = -1.2$ pixels. Part of the discrepancy probably results from the automatic limb-fitting routine that can fail in the presence of active regions near the limb. The discrepancy in the solar radius has a more fundamental reason related to the problem of defining the radius of a fuzzy EUV limb, which is moreover found to be asymmetric in equator and polar direction (Zhang, White, & Kundu 1998). The EIT pixel size of $\Delta x = 2''.616$ is derived for a spacecraft distance of $d = 0.01$ AU from Earth and based on the assumption that the solar limb seen in EIT 171 Å corresponds to the top of the chromosphere ($h =$ 2500 km).

2.2. *Dynamic Stereoscopy Method*

In order to analyze the three-dimensional structure of coronal loops we develop a new technique we might call dynamic stereoscopy, as opposed to static stereoscopy, where the solar rotation is used to vary the aspect angle of otherwise *static* structures (e.g., Loughhead, Chen, & Wang 1984; Berton & Sakurai 1985; Aschwanden & Bastian 1994a, 1994b; Davila 1994; Aschwanden et al. 1995; Aschwanden 1995). The innovative feature of this new technique is that spatial structures, e.g., coronal loops, are allowed to evolve dynamically during the time interval over which the stereoscopic correlation is performed.

In the dynamic stereoscopy method we take advantage of the fact that the global magnetic field is slowly evolving (say during a day) compared with heating and cooling processes in coronal loops. Consequently, the coronal magnetic field $\boldsymbol{B}(\boldsymbol{x}, t)$ can be considered as invariant over short timescales, whereas the confined plasma can flow through "magnetic conduits" in a highly dynamic manner. If a specific coronal flux tube following a field line $\boldsymbol{B}(\boldsymbol{x}, t_1)$ is loaded with bright plasma at time t_1, the same flux tube may be cooled down at time t_2 (say a few hours later) and invisible at the same observed wavelength, whereas heating may occur in an adjacent flux tube $\boldsymbol{B}(\boldsymbol{x} + \Delta \boldsymbol{x}, t_2)$, which was dark at time t_1 and appears now bright at time t_2. For adjacent flux tubes, the two field lines $\boldsymbol{B}(\boldsymbol{x})$ and $\boldsymbol{B}(\boldsymbol{x} + \Delta \boldsymbol{x})$ will run almost parallel, a property we will exploit in our dynamic stereoscopy method. Our method is applicable to coronal structures that meet the following two conditions.

1. The global magnetic vector field $B(\boldsymbol{x}, t)$ is static (or slowly varying) during the time interval over which stereoscopic correlations are performed (typically 1 day). The magnetic field can be traced out by optically thin emission (e.g., in SXR or EUV wavelengths).
2. At least one footpoint of an observed coronal loop is identifiable, which can be used as a reference level of the altitude. For EUV emission we assume that the altitude of a loop footpoint is located in the lower corona above the chromosphere, at an altitude of $h_{\rm foot} \approx 2500$ km above the photosphere.

We outline briefly the numerical procedure of our implementation of the dynamic stereoscopy method, and the mathematical coordinate transformations are given in Appendix A. The projected geometry of a loop segment in an image at time t_1 is traced out by a series of image coordinates (x_i, y_i), $i = 1, \ldots, n$, starting at footpoint position (x_1, y_1), assumed to be anchored at height $h_{\rm foot}$ (Fig. 2). Two additional variables to characterize the three-dimensional geometry of the loop segment are the azimuth angle α of the footpoint baseline and the inclination angle ϑ of the mean loop plane (intersecting the footpoint baseline; see Fig. 2). The procedure of stereoscopic correlation (illustrated in Fig. 3) includes the following steps.

1. Measuring of positions (x_i, y_i), $i = 1, \ldots, n_j$ by tracing a loop segment in an image recorded at time t_1, starting with the primary footpoint at (x_1, y_1).
2. Estimating the position of the secondary footpoint (x_{F_2}, y_{F_2}) to obtain the azimuth angle α of the footpoint baseline. If the full length of the loop can be traced, the secondary footpoint is just given by the last point x_n, y_n, and the tangent of the azimuth angle α corresponds to the ratio of the latitude $(b_{F_2} - b_{F_1})$ and longitude difference $(l_{F_2} - l_{F_1})$ of the two footpoints, i.e.,

$$\tan \alpha = \frac{(b_{F_2} - b_{F_1})}{(l_{F_2} - l_{F_1})} . \quad (1)$$

However, most of the loops analyzed here can only be reliably traced over 1 density scale height, whereas the apex segment is generally so weak that some uncertainty results in the localization of the secondary, magnetically conjugate,

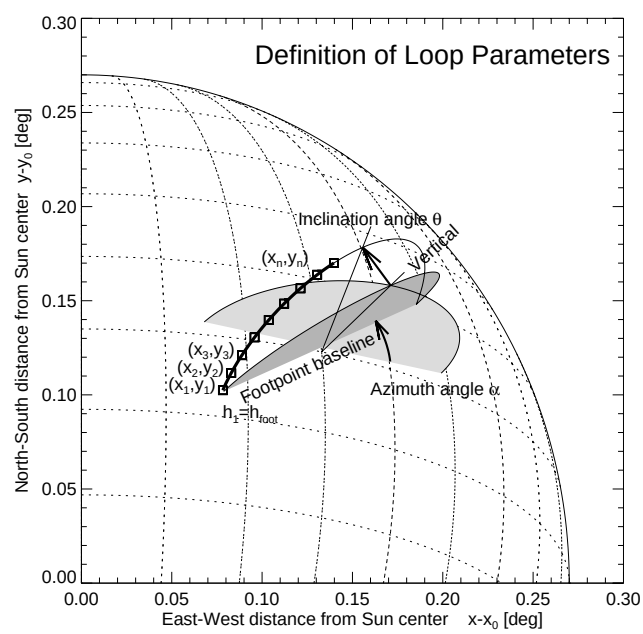

FIG. 2.—Definition of loop parameters: loop point positions (x_i, y_i), $i = 1, \ldots, n$ starting at the primary footpoint at height $h_1 = h_{\rm foot}$, the azimuth angle α between the loop footpoint baseline and heliographic east-west direction, and the inclination angle ϑ between the loop plane and the vertical to the solar surface.

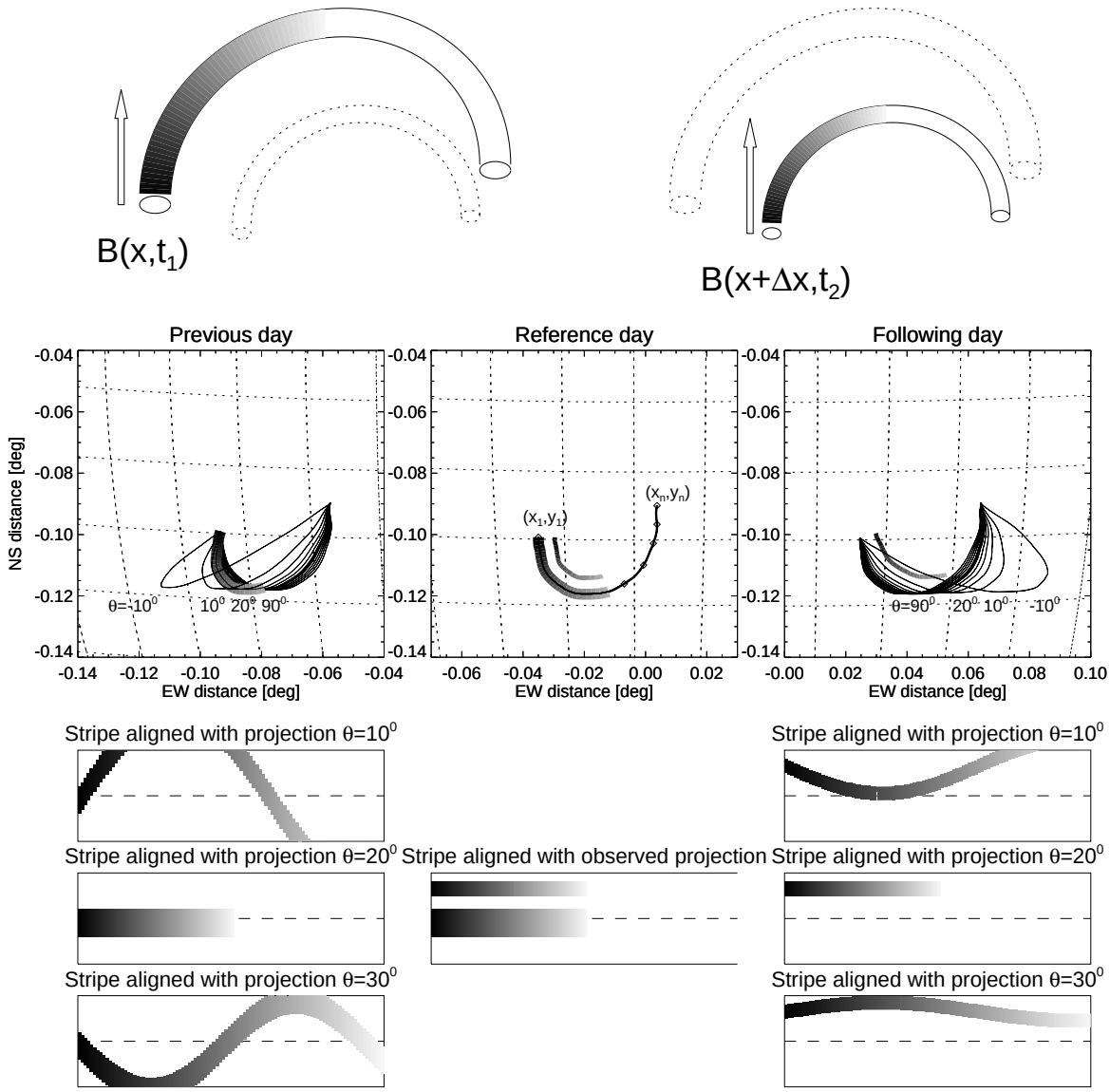

FIG. 3.—Principle of dynamic stereoscopy is illustrated here with an example of two adjacent loops, where a thicker loop is bright at time t_1, whereas a thinner loop is brightest at time t_2. From the loop positions (x_i, y_i) measured at an intermediate reference time t, i.e., $t_1 < t < t_2$ (*middle panel in middle row*), projections are calculated for the previous and following days for different inclination angles ϑ of the loop plane (*left and right panel in middle row*). By extracting stripes parallel to the calculated projections $\vartheta = 10°, 20°, 30°$ (*bottom*) it can be seen that both loops appear only co-aligned with the stripe axis for the correct projection angle $\vartheta = 20°$, regardless of the footpoint displacement Δx between the two loops. The co-alignment criterion can therefore be used to constrain the correct inclination angle ϑ, even for dynamically changing loops.

footpoint. However, the general dipole characteristic of the magnetic field in this active region provides sufficient guidance to localize the secondary footpoint with an accuracy of $\lesssim 10\%$ of the loop length. In order to obtain an error estimate of the location of the secondary footpoint, we repeat the loop tracing procedure five times for each loop and obtain from the measured azimuth angles a_j, $j = 1, \ldots, 5$ a mean and standard deviation $\alpha \pm d\alpha$.

3. The loop positions (x_i, y_i) measured in the image at time t_1 are then transformed into heliographic longitude and latitude coordinates (l_{ij}, b_{ij}) and altitudes (h_{ij}), based on the azimuth angle α of the footpoint baseline and the variable inclination angle ϑ_j, which is varied over a range of $-90° < \vartheta_j < +90°$ in increments of $\Delta\vartheta = 1°$.

4. The heliographic coordinate $l_{ij}(t_1)$ is then transformed to the time t_2 of the second stereoscopic pair image, $l'_{ij}(t_2)$, using the solar differential rotation rate applied to the time interval $(t_2 - t_1)$. We use the differential rotation rate specified by Allen (1973),

$$l'(t_2) = l(t_1) + [13.°45 - 3° \sin^2 b] \frac{(t_2 - t_1)}{1 \text{ day}} . \qquad (2)$$

The heliographic latitude b_{ij} and altitude h_{ij} are assumed to be constant during the considered time interval.

5. In the stereoscopic pair image at time t_2 we calculate the image coordinates (x'_{ij}, y'_{ij}) of the projected loop structure. Parallel to these loop curves (with typical lengths of $n_s = 50$–200 pixels) we extract image stripes of some width ($n_w = 16$ pixels) by interpolating the image brightness $F(x, y)$ at the positions of the curved coordinate grid.

6. The stretched two-dimensional image stripes ($n_s \times n_w$ pixels) are then scanned for parallel brightness ridges, caused by "dynamic" structures that are co-aligned (or parallel-displaced) to the loop projection in image t_2 (for

illustration see examples shown in Fig. 3, *bottom*). This scanning process is numerically performed by measuring the total lengths $L(\vartheta_k)$ of parallel contiguous brightness ridges detected in each image stripe k for a given angle ϑ_k. As the examples in Figure 3 (*bottom*) show, loop projections in stripes with angles ϑ (e.g., $\vartheta = 10°$ or 30°) that deviate from the mean loop plane $\vartheta = 20°$) appear as curved features and thus have shorter parallel segments than those projections in stripes with inclination angles that coincide with the mean loop plane ($\vartheta = 20°$). The numerical detection of the length of parallel segments is therefore a reliable indicator of whether the inclination angle ϑ_k used in the coordinate transformation matches the effective loop plane ϑ. We evaluate this criterion in our algorithm by maximizing the sum of all detected contiguous parallel brightness ridges, i.e., by maximizing the quantity (max $[\sum L(\vartheta_k)]$) as a function of the variable inclination angle ϑ_k used in the coordinate transformation. This way we infer the most likely value of the inclination angle ϑ of the mean loop plane.

7. The same procedure is repeated in forward and backward directions in time. The mean and standard deviation of $\vartheta \pm d\vartheta$ is determined by averaging the two stereoscopic solutions (± 1 day).

The independent stereoscopic correlation in forward ($+1$ day) and backward (-1 day) direction provides a useful redundancy of the solution. The time difference of ± 1 day corresponds to an aspect angle change of $\pm 13\overset{\circ}{.}5$. Except for steps 1–2, which constitute the definition of a selected loop feature, all other steps (3–7) of the stereoscopic correlation are performed automatically by a numeric code without human interaction. The determination of the loop inclination angle ϑ is therefore achieved in a most objective way, within the principle of dynamic stereoscopy.

2.3. *Loop Geometry*

With the dynamic stereoscopy method described above we analyzed the three-dimensional coordinates of 30 loops from the EIT 171 Å image on 1996 August 30 (Fig. 4, *middle column*). The true three-dimensional geometry of (the central axis of) a coronal loop can be characterized with three orthogonal spatial coordinates $[x(s_i), y(s_i), z(s_i)]$, $i = 1, \ldots, n$, parametrized by the loop length parameter s_i. When we trace a loop structure in an image (see Fig. 4, *middle column*), we can accurately measure the two coordinates $[x(s_i), y(s_i)]$, without imposing any geometric constraint on its shape, as opposed to a method that fits a predefined geometric model (e.g., a circular geometry or its elliptic projection). We impose only some constraints on the third coordinate $z(s_i)$, namely, assuming that the loop segment is mathematically described in a plane, whose orientation we quantify with two free parameters (Fig. 2): with the azimuth angle α (of the loop footpoint baseline) and the stereoscopically measured inclination angle ϑ (with respect to the

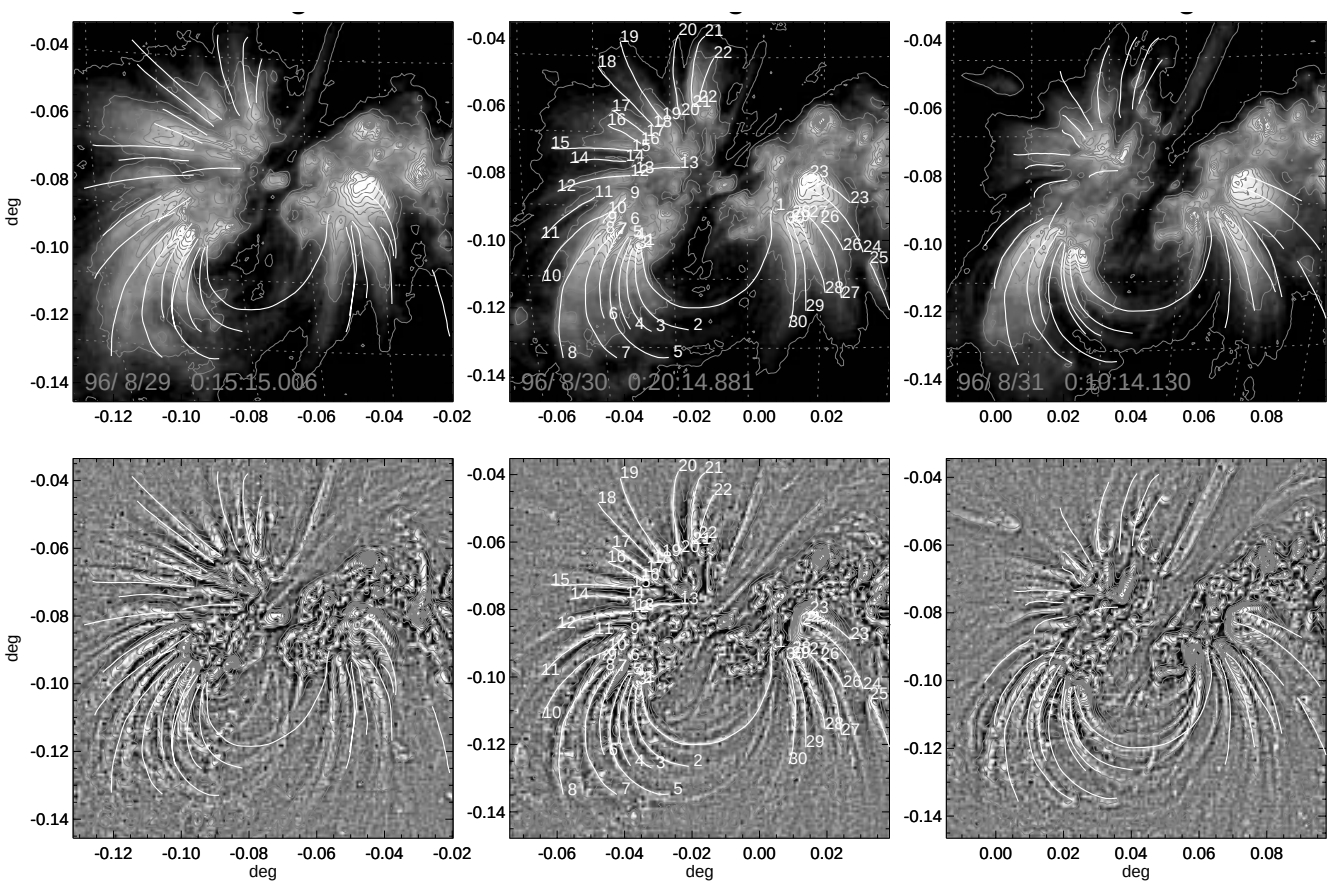

FIG. 4.—Projections of 30 stereoscopically reconstructed loop segments (numbered white curves) are shown overlaid on the *SOHO*/EIT 171 Å images (*top*) and the filtered images (*bottom*) of 1998 August 29 (*left*), 30 (*center*), and 31 (*right*). The 30 loop segments were traced from the filter image of August 30 (*bottom middle*), whereas the projections on the previous and following day were calculated from the inclination angles ϑ obtained from the dynamic stereoscopy method. Note that the overall magnetic field structure is almost invariant during the 3 days, but dynamic changes of the loops produce slight displacements between the calculated projections forward and backward in time and the actually observed fine structure.

vertical). However, the planar approximation serves only for mathematical convenience and defines a mean loop plane but does not require that the actual loop is exactly confined in a plane because our dynamic stereoscopy method allows for near-parallel displacements in time and space within some range. One additional constraint is also introduced by the reference level $h(s_1)$ of the first footpoint position, assumed to be located at a fixed height of $h(s_1) = h_{\rm foot} \approx 2.5$ Mm.

Some geometric elements of the analyzed 30 loops are listed in Table 1: the heliographic longitude (l_1) and latitude (b_1) position of the primary footpoint [$x(s_1)$, $y(s_1)$, $h(s_1) = h_{\rm foot}$], the azimuth angle α of the footpoint baseline measured at the primary footpoint, and the inclination angle ϑ of the loop plane. The average heliographic position of the 30 loop footpoints is $\langle l_{F_1} \rangle = 251\overset{\circ}{.}0$, $\langle b_{F_1} \rangle = -11\overset{\circ}{.}8$, which is slightly southward of the Sun center position at this time, $l_0 = 255\overset{\circ}{.}8$, $b_0 = 7\overset{\circ}{.}2$.

The average azimuth angle (modulo 180°) of the 30 loop footpoint baselines is $\alpha = -3° \pm 10°$, which represents the global orientation of the large-scale dipolar magnetic field that dominates the active region, which was used as a guide to estimate the azimuth angle of the footpoint baseline for individual loop segments. The only complete loop that could be traced out (without gaps between the footpoints) is loop 1, which has an azimuth angle of $\alpha = 15° \pm 1°$.

The inclination angles ϑ of the loop planes cover a large range from $\vartheta = -56°$ to $\vartheta = +69°$, having an average of $\langle \vartheta \rangle = 7° \pm 37°$. The southern loops (loops 1–11, 23–30) all show an inclination toward south (with ϑ negative if the primary footpoint is to the east), whereas the northern loops (loops 12–22) show a systematic inclination toward north (with ϑ positive if the primary footpoint is to the east). This fan-shaped divergence of loop planes is consistent with the overall magnetic dipolar field, having the dipole axis aligned to the east-west direction.

We visualize the three-dimensional structure of the stereoscopically reconstructed 30 loops in Figure 5, where different perspectives and viewing angles are displayed. The traced segments (Fig. 4) of the reconstructed loops are marked with thick lines in Figure 5, whereas the thin lines represent circular segments in the loop plane, constrained by the two footpoints and the endpoint of the traced segment. We rotated these reconstructed 30 loops by -7.2 days to the east (Fig. 5, *bottom left*), in order to illustrate the distribution of inclination angles. The group of loops that are inclined to the south in our EIT image of 1996 August 30 are also found to have a similar configuration (with similar loop heights and loop plane inclinations) in an EIT image observed 7.2 days earlier, when this active region crossed the east limb (Fig. 5, *top left*).

2.4. *Loop Background Subtraction*

We parametrize the positions of the traced loop segments from the image coordinates [$x(s_i)$, $y(s_i)$] as a function of the (projected) loop length parameter s_i, by interpolating the

TABLE 1

GEOMETRIC PARAMETERS OF 30 CORONAL LOOPS (1996 AUGUST 29, EIT 171 Å)

Loop Number	Heliographic Coordinates l_1, b_1 (deg)	Azimuth Angle α (deg)	Inclination Angle ϑ (deg)	Loop Radius R_0 (Mm)	Center Offset Z_0 (Mm)	Loop Trace L_1 (Mm)	Loop Length L (Mm)	Scale Height λ (Mm)	Loop Width w (Mm)
1	247.9, −15.4	15 ± 1	−42 ± 1	56	−14	149	149	49	6.8
2	247.7, −15.5	13 ± 1	−49 ± 5	62	18	91	234	50	6.1
3	247.4, −15.6	12 ± 1	−34 ± 1	68	31	89	282	57	7.4
4	247.3, −15.0	8 ± 2	−26 ± 1	77	45	104	338	57	6.9
5	247.1, −14.9	8 ± 3	−49 ± 1	73	37	121	309	56	6.3
6	247.0, −13.9	2 ± 2	−56 ± 1	84	53	80	381	42	7.0
7	246.1, −14.7	4 ± 2	−36 ± 1	89	51	125	389	62	7.1
8	245.2, −14.7	9 ± 2	−33 ± 2	113	80	124	534	57	7.1
9	247.0, −12.2	−3 ± 3	−12 ± 1	86	44	41	366	60	8.1
10	245.8, −13.3	1 ± 2	−23 ± 1	124	95	90	609	53	7.9
11	244.9, −12.2	1 ± 3	−31 ± 2	144	116	56	725	66	6.8
12	247.3, −10.7	−6 ± 2	10 ± 1	116	94	153	585	60	7.8
13	250.6, −10.1	−9 ± 7	11 ± 1	73	60	62	373	60	6.4
14	247.1, −9.8	−8 ± 3	10 ± 1	113	87	70	554	33	6.4
15	247.5, −9.0	−8 ± 1	12 ± 1	125	105	103	643	47	6.8
16	248.1, −8.5	−11 ± 3	25 ± 1	85	59	63	400	53	6.7
17	248.5, −8.0	−14 ± 4	32 ± 1	93	71	52	455	47	7.4
18	249.0, −7.4	−9 ± 4	40 ± 3	92	79	109	483	93	5.6
19	249.6, −6.9	−18 ± 3	39 ± 1	116	95	130	590	65	7.9
20	250.7, −6.6	−24 ± 6	52 ± 6	78	64	103	399	56	7.7
21	251.5, −6.1	−21 ± 6	58 ± 3	67	47	85	318	45	7.6
22	251.9, −5.7	−25 ± 5	58 ± 3	49	29	53	217	58	7.2
23	259.1, −10.7	−4 ± 4	0 ± 1	102	71	69	479	60	8.0
24	258.6, −11.4	−1 ± 4	14 ± 6	114	90	106	568	64	8.7
25	263.2, −16.6	−1 ± 5	43 ± 1	138	70	59	582	42	8.1
26	259.9, −13.8	−8 ± 4	13 ± 2	100	60	39	446	59	5.1
27	259.1, −13.4	−2 ± 3	50 ± 2	101	68	72	471	58	7.1
28	258.0, −13.4	0 ± 2	27 ± 2	90	63	86	423	57	7.5
29	257.9, −13.7	5 ± 2	36 ± 1	78	45	88	344	60	6.0
30	257.5, −13.8	−2 ± 3	69 ± 1	76	44	86	336	38	7.4
Average...	251.0 (±5.4), −11.8 (±3.3)	−3 (±10)	7 (±37)	93 (±23)	62 (±27)	89 (±29)	433 (±136)	55 (±10)	7.1 (±0.8)

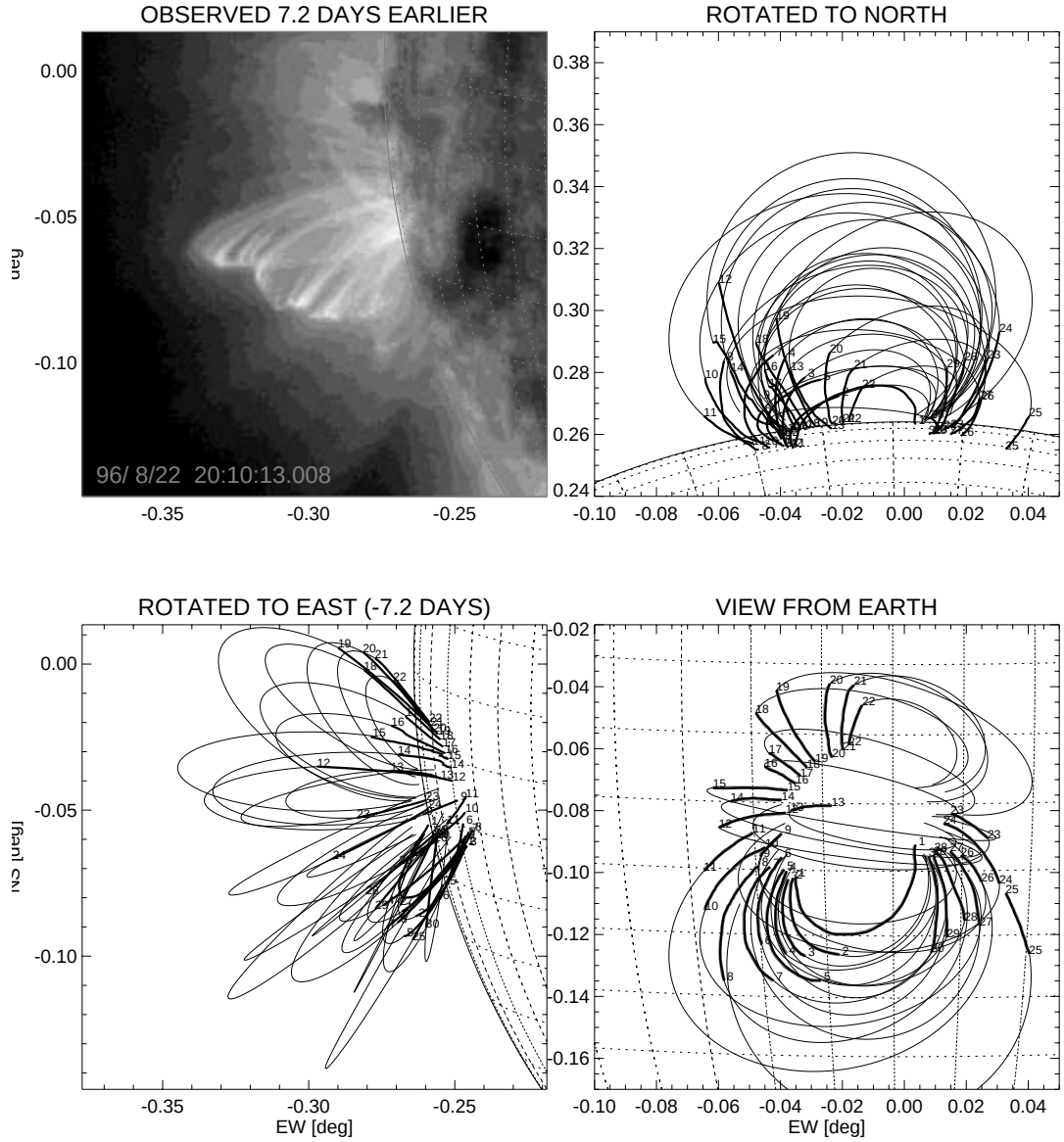

FIG. 5.—Three different projections of the stereoscopically reconstructed 30 loops of AR 7986 are shown. The loop segments that were traced from the 1996 August 30, 171 Å image are marked with thick solid lines, whereas the extrapolated segments (*thin solid lines*) represent circular geometries extrapolated from the traced segments. The three views are (1) as observed from Earth with l_0, b_0 (*bottom right*), (2) rotated to north by $b'_0 = b_0 - 100°$ (*top right*), and (3) rotated to east by $l'_0 = l_0 + 97.^\circ 2$ (corresponding to -7.2 days of solar rotation, *bottom left*). An EIT 171 Å image observed at the same time (-7.2 days earlier) is shown for comparison (*top left*), illustrating a similar range of inclination angles and loop heights as found from stereoscopic correlations a week later. The heliographic grid has a spacing of 5° degrees or 60 Mm.

coordinates with a constant resolution of $\Delta s_i = s_{i+1} - s_i =$ 1 pixel in the image plane. These positions mark the central axes of the analyzed loops. For single-loop analysis it is convenient to introduce a coordinate grid $[s_i, t_j]$ that is co-aligned with the loop axis s_j, and t_j is the coordinate orthogonal to the loop axis. The projections $[x(s_i, t_j), y(s_i, t_j)]$ of these curved coordinate grids are shown in Figure 6 (*top right*). We parametrized both coordinates $[s_i, t_j]$ with a uniform resolution of 1 pixel and have chosen a width of 16 pixels for the width of the stripes (t_j), symmetrically bracketing the central loop axis. We show the radiative flux $F(t_j)$ as a function of the loop cross section t_j for each loop (1–30) and for each position s_i along the central loop axis with an incremental step of $\Delta s_i = 1$ pixel in Figure 6, measured from the EIT 171 Å image of 1996 August 30.

In a next step we attempt to separate the loop-associated fluxes from the loop-unrelated background. This is a very crucial step to determine the correct emission measure and electron density in a given loop. This task is difficult because most of the loops are very closely spaced and separated only by a few pixels at their primary footpoint (see Fig. 6). Very few loops occur in an isolated environment (e.g., such as loop 25; see Figs. 4–6). For many cross sections there is not enough separation between adjacent loops to model the loop-unrelated background properly. The fact that the flux-unrelated background makes up typically 50%–90% of the total EUV flux measured at a given line of sight (see Fig. 7) indicates that we can separate out only a fraction of superposed and nested loops, like the topmost elements on the topological surface of a "strand of spaghetti."

We tested various methods and found the following to be least susceptible to confusion by adjacent loops. We calculated the background profile $F_B(t_j)$ to the observed flux $F(t_j)$

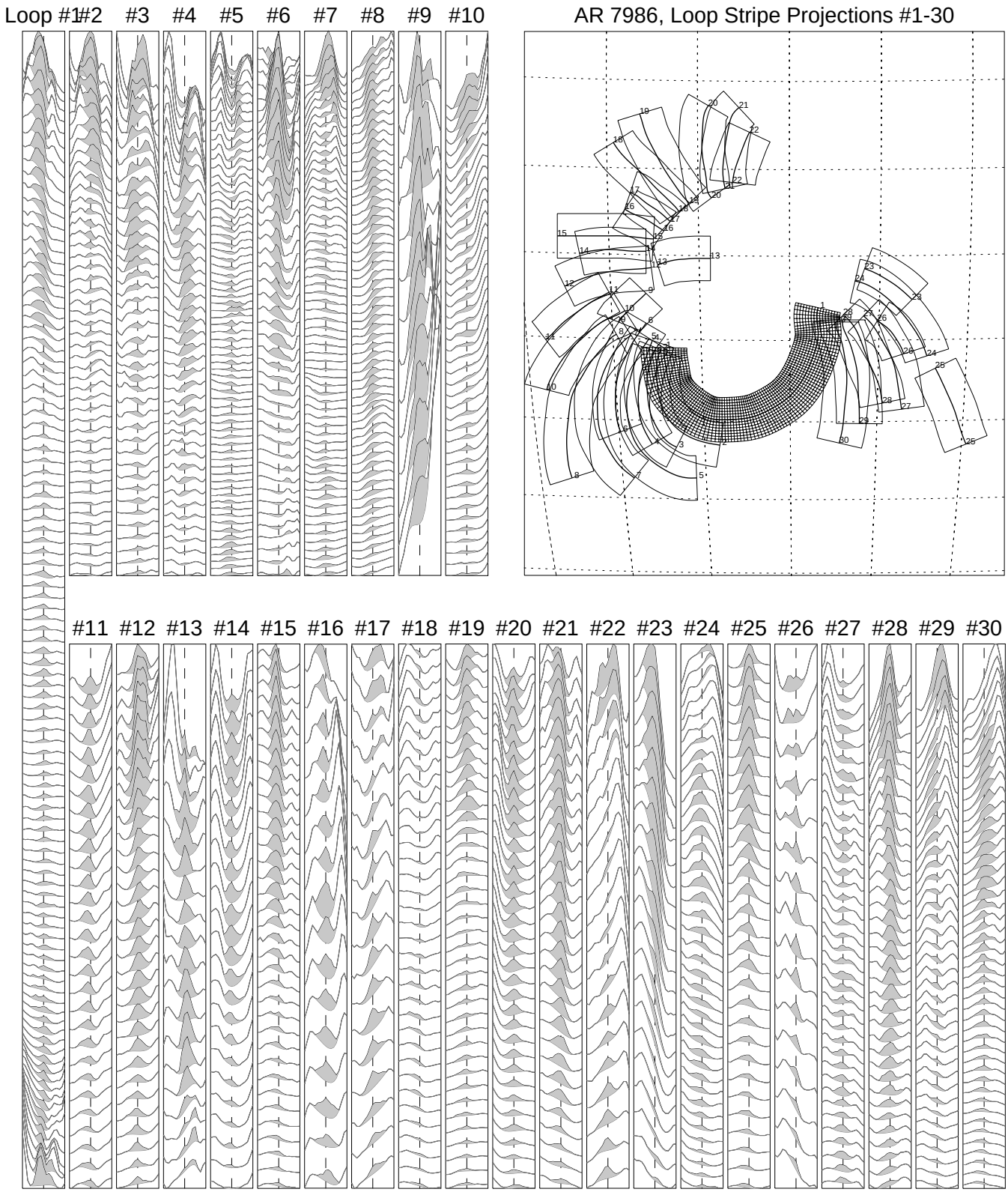

FIG. 6.—Positions of the curved coordinate grids of the 30 analyzed loop segments are shown in the top right panel, which has the same orientation as the 1996 August 30 map shown in Fig. 4 (*middle*). The coordinate grid of loop 1 is represented with 1 pixel resolution, whereas only the outer borders and central axes are indicated for the other loop segments. The vertically oriented panels represent the coordinate grids of the analyzed 30 loops, stretched out along the loop axis. The top of the panels corresponds to the primary footpoint (see positions l_1, b_1 in Table 1). In each panel we show the EIT 171 Å flux loop cross sections measured perpendicularly to the loop axes. Successive cross sections are separated by a distance of 1 pixel along the loop axis. The flux associated with each loop is marked with a gray area, obtained by background subtraction with a cubic spline interpolation between both sides of the loop cross section.

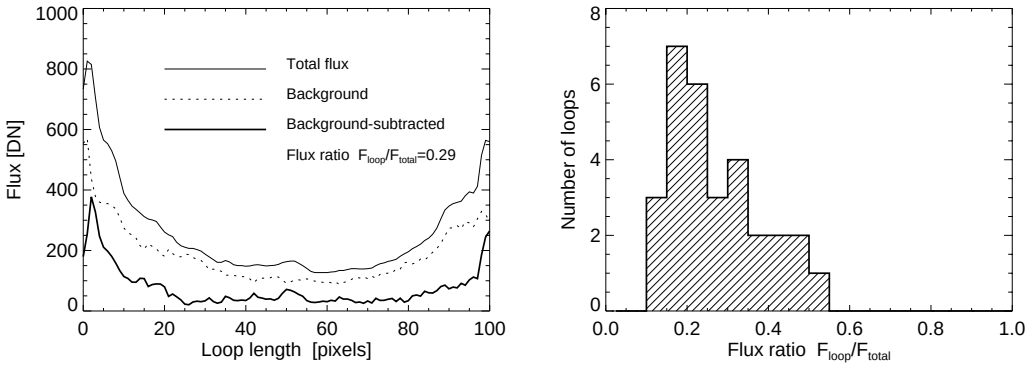

FIG. 7.—Loop-associated EUV flux [$F_{loop}(s)$, *thick line*], the total EUV flux [$F_{total}(s)$, *thin line*], and the background [$F_{total}(s) - F_{flux}(s)$, *dotted line*] measured along the loop is shown for loop 1 (*left*). A histogram of the relative fractions F_{loop}/F_{total} (integrated over the traced loop lengths) is shown from all 30 analyzed loops (*right*).

by cubic spline interpolation between various cross section boundaries $[t_1, t_2]$, which were varied over a range of 1, ..., 4 pixels (or 2–7 Mm for the half-width of the loop cross section) on both sides of the central loop axis. From the varied loop boundaries $[t_1, t_2]$ those were used for the background envelope that maximize the flux integrated over loop cross section, i.e., the maximum of $\int [F(t_j) - F_B(t_j)]dt_j$ because this quantity is invariant to lateral displacements (in transverse direction t) and is least susceptible to changes of the functional form $F(t)$ along the loop coordinate s. This method has the advantage of adjusting for loop thickness variations, for offsets in tracing of the central axis, and for co-alignment errors between the 171 and 195 Å image in the use of the filter-ratio technique. The so-determined loop-associated fluxes are shown with gray areas for each cross section $F(t_j)|_{s=s_i}$ in Figure 6. The results show that the allowed loop half-width range of $\pm 1, \ldots, 4$ pixels separates most of the loops reasonably, except for occasional double loop detections (e.g., 22 or 26 in Fig. 6) near the primary footpoint. Such loop segments where the loop separation fails will be excluded in further analysis.

2.5. *Loop Cross Sections*

We measured the loop width $w(s)$ as a function of the loop length parameter s, using the definition of the *equivalent width* $w(s)$,

$$w(s) = \frac{\int F(s, t_j) - F_B(s, t_j)\, dt_j}{\max\, [F(s, t_j) - F_B(s, t_j)]} . \quad (3)$$

These loop widths $w(s)$ are shown as a function of the loop length s in Figure 8 for the 10 loops that are least confused by adjacent loops, as can be judged from the cross sections $F(t_j)|_{s=s_i}$ shown in Figure 6 (loop 1, 8, 11, 14, 15, 19, 20, 21, 25, 28). Performing a linear regression fitted to the observed values $w(s)$, we find a significant variation of the loop thickness only for two of them (loop 20 and 28). To quantify the variation of the loop thickness we calculated a *loop divergence factor*, defined by the average width in the upper part ($s_{max}/2 < s < s_{max}$) to the lower part ($0 < s < s_{max}/2$) of the traced loop segment. We remind the reader that the traced loop segments generally extend over about 1 density scale height but often do not reach the loop top (except for the smallest loop, 1). The loop divergence factors and their uncertainties are shown in Figure 8 (*bottom right*) for each loop. We caution that some of the loop thickness variation near the footpoints is due to separation problems of closely spaced adjacent loops (as can be judged from Fig. 6). A histogram of average loop widths is shown in Figure 8 (*top right*), whereas the individual values w and their mean and standard deviation ($w = 7100 \pm 800$ km) are also listed in Table 1. The preference for such a narrow range of loop diameters is perhaps an instrumental resolution bias because the finest recognizable structures are most likely to be seen at a scale corresponding to the size of a few pixels.

2.6. *Loop Densities and Scale Heights*

For electron density and temperature diagnostics we are using a filter-ratio technique applied to the EIT 171 and 195 Å wavelength images, based on the most recent EIT standard software (status of 1998 February, Newmark et al. 1996; *SOHO* EIT User's Guide). The resulting emission measures EM and temperatures T_e^{EIT} are based on the calculation of synthetic spectra using the CHIANTI database, containing some 1400 emission lines in the 150–400 Å wavelength range (Dere et al. 1997). For details of the EIT calibration and error analysis, the reader is referred to Delaboudinière et al. (1995), Moses et al. (1997), and Neupert et al. (1998). Further cross calibrations of the EIT instrument with NRL rocket flights carrying an EIT duplicate instrument are in progress (led by D. Moses). In brief, we note that the main errors at this stage are systematic and due to calibration questions. This has a larger effect on the emission measure than on the temperature because the latter is determined from a ratio, in which systematic errors cancel out to some extent. Our estimate of the absolute error in the temperature determination is about 0.2 MK, whereas the emission measure has a systematic error of up to a factor of 4. The abundances in the above calculations are those given by Meyer (1985) for the corona. As iron is a low–first ionization potential (FIP) element, abundance questions play a minor role in the uncertainties.

To determine the electron density $n_e(s)$ along individual loops, we use the background-subtracted EIT fluxes $F_{loop}(s) = F(s) - F_B(s)$ in the filter ratios and the loop widths $w(s)$. An additional important loop parameter is the line-of-sight angle $\psi(s)$, which provides a correction factor of the effective column depth for a loop with circular cross section specified by a diameter $w(s)$, i.e., $w_z(s) = w(s)/\cos\,[\psi(s)]$ (see Appendix B). With this parametrization we define the density $n_e(s)$ along a loop (normalized to a filling factor of unity) by

$$n_e(s) = \sqrt{\frac{\mathrm{EM}(s)}{w_z(s)}} = \sqrt{\frac{\mathrm{EM}(s)\,\cos\,[\psi(s)]}{w(s)}} , \quad (4)$$

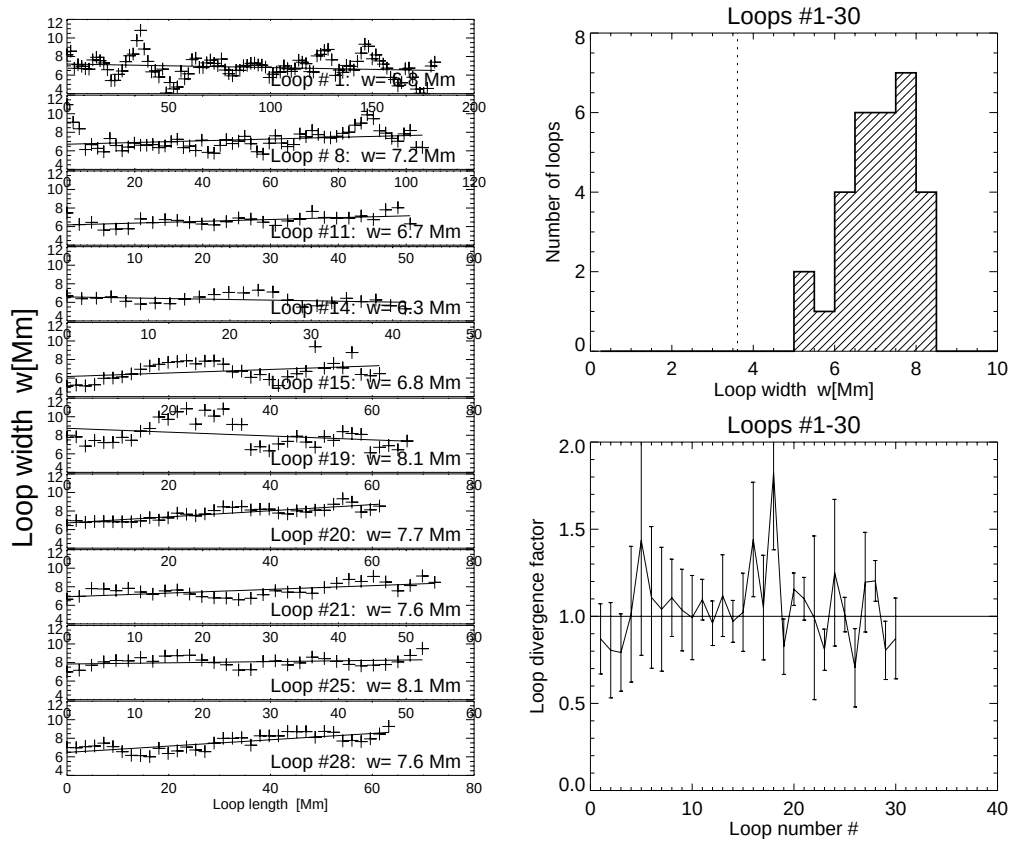

FIG. 8.—Variation of the loop thickness is shown for the 10 loops with the least confusion by adjacent loops (see cross sections in Fig. 6) as a function of the loop length s (*left*). A linear regression fit is indicated (*solid line in left panels*). The average (equivalent) width w is histogrammed for all 30 analyzed loops (*top right*). A loop divergence factor is calculated from the ratio of the average width in the upper half and lower half (*traced*) loop segments (*right bottom*). Note that most of the loops show no significant loop thickness variation.

with the loop length $s(x, y)$ parametrized as a function of the image position (x, y), from which the EIT emission measure $\mathrm{EM}(x, y)$ is measured. Because the line-of-sight angle $\psi(s)$ is very sensitive to the loop orientation, correct values of the electron density $n_e(s)$ can only be obtained from an appropriate three-dimensional model of the loop (constrained by stereoscopic correlations here). The projection effect of the loop curvature on the effective column depth $w_z(s)$, and the effect of the inclination angle ϑ of the loop plane on the inferred density scale height $\lambda(\vartheta)$ are illustrated in Figure 9 (see also discussion in Alexander & Katsev 1996).

The electron density $n_e(s)$ calculated from equation (4) is shown graphically for the 10 least-confused loops (1, 8, 11, 14, 15, 19, 20, 21, 25, 28) in Figure 10 (*left*). Because the height dependence $s(h)$ of the loop length is known from our stereoscopic reconstruction (displayed in Fig. 5), we can directly obtain the parametrization $n_e[s(h)] \mapsto n_e(h)$ and fit an exponential density model,

$$n_e(h) = n_{e0} \exp\left[-\frac{h}{\lambda(T_e)}\right] \tag{5}$$

to obtain a scale height temperature T_e^{λ}, which is defined by (e.g., Lang 1980, p. 285)

$$\lambda(T_e) = \frac{k_{\mathrm{B}}\, T_e}{\mu m_{\mathrm{H}}\, g} \approx 46\left(\frac{T_e}{1\ \mathrm{MK}}\right)[\mathrm{Mm}]\ , \tag{6}$$

with k_{B} the Boltzmann constant, μ the mean molecular weight ($\mu \approx 1.4$ for the solar corona), m_{H} the mass of the hydrogen atom, and g the acceleration of gravity at the solar surface. The so obtained scale height λ, with a mean of $\lambda = 55 \pm 10$ Mm, and the inferred scale height temperature T_e^{λ}, with a mean of $T_e^{\lambda} = 1.22 \pm 0.23$, are listed in Tables 1 and 2 for each of the analyzed 30 loops. Loop segment ranges that are obviously confused by adjacent or crossing loops (as can be judged from Fig. 6), have been excluded in the fitting of the scale height model. We find that most of the analyzed loop segments fit closely an exponential density model (see Fig. 10, *left*). Deviations from an exponential density model can often be explained by uncertainties in the background subtraction or by confusion from adjacent or overlying loops. A correction to the local scale height temperature would also result from temperature gradients (§ 2.8), which are of the order $(dT/ds)/(T/\lambda) \approx 0.05 \pm 0.20$ and are neglected here.

2.7. *Loop Temperatures*

Independently of the scale height temperature T_e^{λ}, we can also determine the temperature directly from the EIT filter ratio (as described in § 2.6), which moreover provides a temperature differentiation along the loop, $T_e^{\mathrm{EIT}}(s)$. Since our loop definitions are based on tracing of an EIT 171 Å image, we use only the filter ratio of EIT 171 Å (Fe IX, Fe X) and 195 Å (Fe XII), which is sensitive in the temperature regime of $T_e = 1.0$–1.5 MK. We are using the spatial loop definition $[x(s), y(s)]$ based on the 171 Å image and apply the same background-subtraction technique to the 195 Å

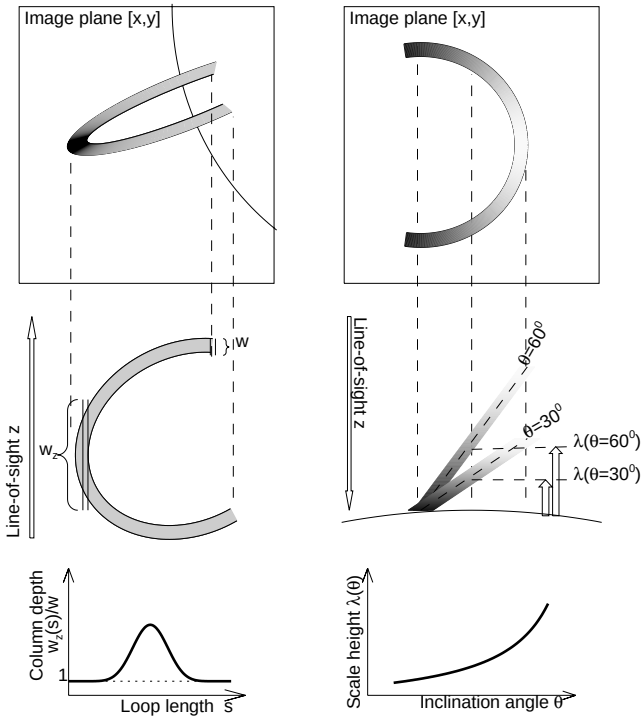

FIG. 9.—*Left:* The effect of the variable column depth $w_z(s)$ measured parallel to the line of sight z is illustrated as a function of the loop length parameter s, for a loop with a constant diameter w. *Right:* The effect of the inclination angle ϑ of the loop plane on the inferred density scale height $\lambda(\vartheta)$ is shown. Both effects have to be accounted for the determination of the electron density $n_e(s)$ along the loop.

image before we determine the temperature from the filter ratio $(F^{195} - F_B^{195})/(F^{171} - F_B^{171})$. Because our background-subtraction technique has some tolerance (of $\pm 1, \ldots, 4$ pixels) in the localization of the loop cross section (by maximizing the flux integrated over the loop cross section), the filter-ratio is not susceptible to small co-alignment errors between the 171 and 195 Å image. The employed background-subtraction technique also requires a correlated structure (with a width of 2–8 pixels) in both wavelengths, whereas larger or diffuse structures with possibly different temperatures are safely subtracted out.

The filter-ratio temperatures $T_e^{\rm EIT}$ averaged over the loop segments are tabulated in Table 2, with a mean of $T_e^{\rm EIT} = 1.21 \pm 0.06$ MK. The distribution of filter-ratio temperatures $N(T_e^{\rm EIT})$ is shown in Figure 11 (*bottom left*), along with the distribution of scale height temperatures $N(T_e^{\lambda})$ (Fig. 11, *top left*), both having almost identical means. The range of scale height temperatures (± 0.23 MK) is broader than the range of EIT filter-ratio temperatures (± 0.06 MK), probably because of systematic errors in background subtraction and loop separation. This is also consistent with the scatter plot of the two temperature definitions (Fig. 11, *top right*), where no obvious correlation is seen. Despite these unavoidable uncertainties in the background subtraction, it is remarkable that the means of the two independently determined temperatures coincide so closely.

2.8. *Loop Temperature Gradients*

The detailed variation of the temperature $T_e^{\rm EIT}(s)$ along the loop length s is shown for the 10 least-confused loops in

TABLE 2

PHYSICAL PARAMETERS OF 30 CORONAL LOOPS (1996 AUGUST 29, EIT 171 Å)

Loop Number	Emission Measure EM_0 log (cm^{-5})	Electron Density $n_e/10^9$ (cm^{-3})	Scale Height Temperature T_e^{λ} (MK)	Filter-Ratio Temperature $T_e^{\rm EIT}$ (MK)	Temperature Gradient dT/ds (K km^{-1})	Conductive Loss Rate $\nabla F_c \times 10^3$ (ergs cm^{-3} s^{-1})	Radiative Loss Rate $E_R \times 10^3$ (ergs cm^{-3} s^{-1})	Steady State Heating Rate $E_H \times 10^3$ (ergs cm^{-3} s^{-1})	Magnetic Field $B_{\rm foot}$ (G)
1	27.71	2.5	1.08 ± 0.07	1.25 ± 0.09	2.2 ± 0.5	−0.001	−0.718	0.716	−413
2	27.93	2.3	1.09 ± 0.12	1.27 ± 0.10	1.7 ± 1.0	−0.001	−0.607	0.607	−413
3	27.79	2.1	1.25 ± 0.13	1.22 ± 0.10	−0.1 ± 0.8	−0.000	−0.506	0.506	−285
4	27.60	2.6	1.26 ± 0.14	1.27 ± 0.11	3.7 ± 0.8	−0.004	−0.776	0.773	−285
5	27.34	2.5	1.22 ± 0.33	1.23 ± 0.10	−1.1 ± 0.4	−0.000	−0.718	0.718	−270
6	29.68	3.7	0.93 ± 0.08	1.30 ± 0.12	7.9 ± 2.7	−0.015	−1.572	1.557	−298
7	27.88	1.7	1.36 ± 0.17	1.19 ± 0.09	0.9 ± 0.3	−0.000	−0.332	0.332	−261
8	27.45	2.2	1.26 ± 0.10	1.23 ± 0.06	0.9 ± 0.2	−0.000	−0.556	0.555	−114
9	27.52	2.1	1.32 ± 0.53	1.15 ± 0.03	0.6 ± 1.0	−0.000	−0.506	0.506	−333
10	27.49	1.4	1.16 ± 0.30	1.21 ± 0.11	2.2 ± 0.5	−0.001	−0.225	0.224	−148
11	27.11	1.6	1.44 ± 0.18	1.20 ± 0.09	4.9 ± 0.4	−0.006	−0.294	0.288	7
12	27.56	2.0	1.31 ± 0.07	1.10 ± 0.06	0.5 ± 0.2	−0.000	−0.459	0.459	−208
13	27.41	1.8	1.31 ± 0.17	1.21 ± 0.11	4.6 ± 1.3	−0.006	−0.372	0.366	−252
14	27.18	1.7	0.73 ± 0.08	1.12 ± 0.05	1.2 ± 0.7	−0.000	−0.332	0.331	−157
15	27.48	2.0	1.04 ± 0.08	1.18 ± 0.09	1.8 ± 0.3	−0.001	−0.459	0.458	−294
16	27.28	1.4	1.15 ± 0.32	1.24 ± 0.12	−6.4 ± 0.7	−0.000	−0.225	0.225	−269
17	27.04	1.7	1.03 ± 0.30	1.18 ± 0.04	2.2 ± 0.6	−0.001	−0.332	0.330	−178
18	26.90	1.1	2.03 ± 0.41	1.30 ± 0.06	0.7 ± 0.6	−0.000	−0.139	0.139	−159
19	27.28	1.3	1.43 ± 0.17	1.18 ± 0.04	0.0 ± 0.4	−0.000	−0.194	0.194	−129
20	27.43	1.8	1.22 ± 0.05	1.22 ± 0.04	1.2 ± 0.2	−0.000	−0.372	0.372	−140
21	27.51	2.1	0.98 ± 0.11	1.15 ± 0.04	0.8 ± 0.3	−0.000	−0.506	0.506	−97
22	27.32	1.0	1.27 ± 0.82	1.22 ± 0.12	−4.5 ± 1.9	−0.000	−0.115	0.115	−159
23	27.61	2.3	1.31 ± 0.28	1.23 ± 0.15	11.4 ± 1.0	−0.024	−0.607	0.584	54
24	28.29	1.3	1.41 ± 0.22	1.20 ± 0.08	−7.3 ± 4.0	−0.000	−0.194	0.194	951
25	27.38	1.8	0.93 ± 0.04	1.18 ± 0.11	5.4 ± 0.5	−0.007	−0.372	0.365	76
26	26.95	1.4	1.30 ± 0.36	1.15 ± 0.08	5.9 ± 1.8	−0.009	−0.225	0.216	60
27	27.20	1.5	1.26 ± 0.30	1.21 ± 0.07	−1.7 ± 0.5	−0.000	−0.258	0.258	61
28	27.79	2.6	1.24 ± 0.05	1.12 ± 0.04	0.0 ± 0.3	−0.000	−0.776	0.776	128
29	27.76	2.4	1.31 ± 0.06	1.36 ± 0.07	−1.2 ± 0.6	−0.000	−0.661	0.661	128
30	29.48	1.7	0.84 ± 0.10	1.16 ± 0.08	−9.7 ± 4.8	−0.000	−0.332	0.332	142
Average...	27.61 (±0.61)	1.92 (±0.56)	1.22 (±0.23)	1.21 (±0.06)	0.960 (±4.265)	−0.003 (±0.005)	−0.458 (±0.285)	0.455 (±0.283)	−108 (±257)

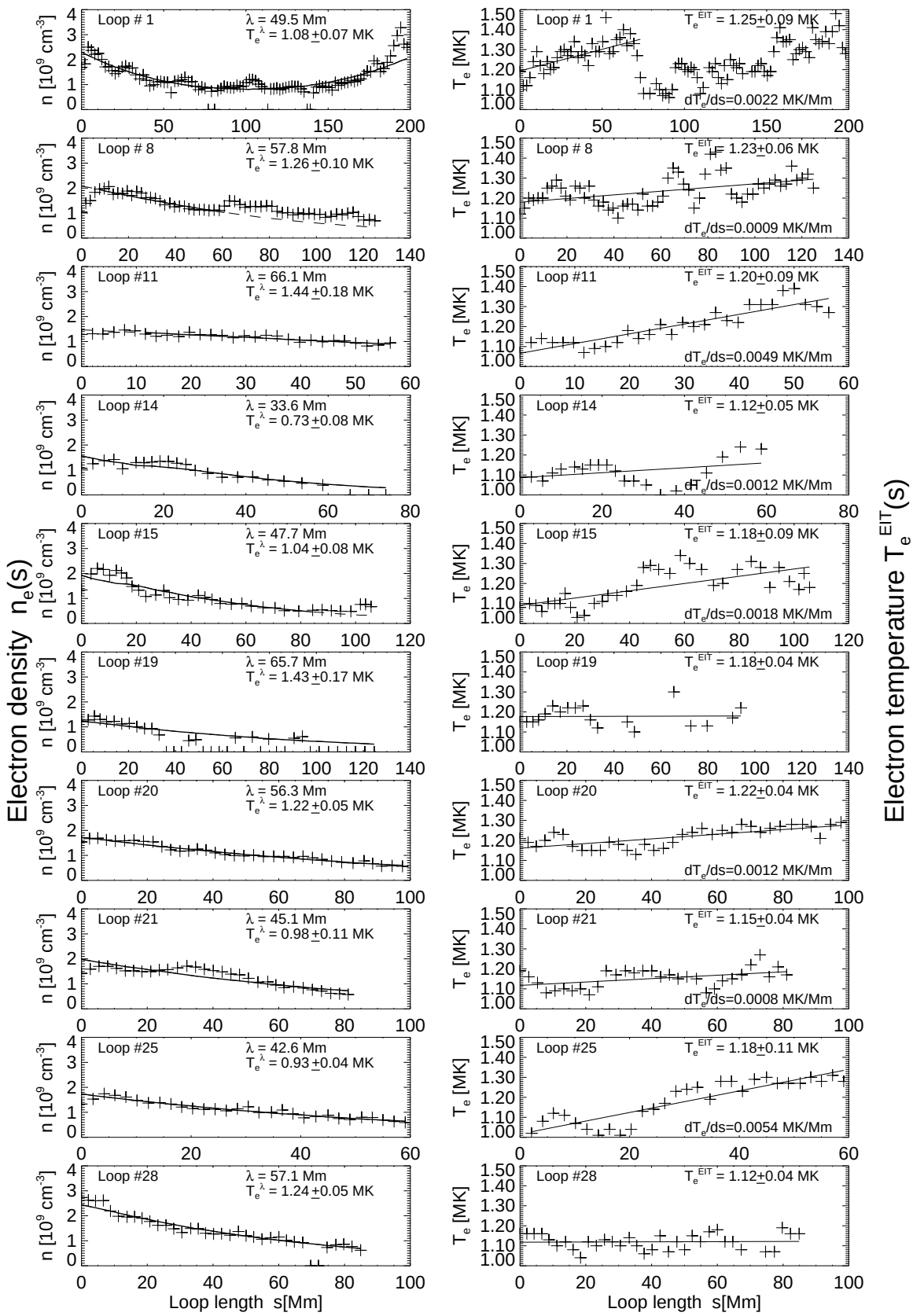

FIG. 10.—Electron density $n_e(s)$ (*left*) and the EIT filter-ratio electron temperature $T_e(s)$ (*right*) as a function of the loop length s for the same 10 loops selected in Fig. 8. An exponential model $n_e(h)$ is fitted, yielding the density scale height λ and scale height temperature T_e^{λ} indicated in the left panels. The average EIT filter-ratio temperature $T_e^{\rm EIT}$ (obtained from 171/195 Å images) is indicated in the right panels. A temperature gradient dT_e/ds is listed if the gradient is significant.

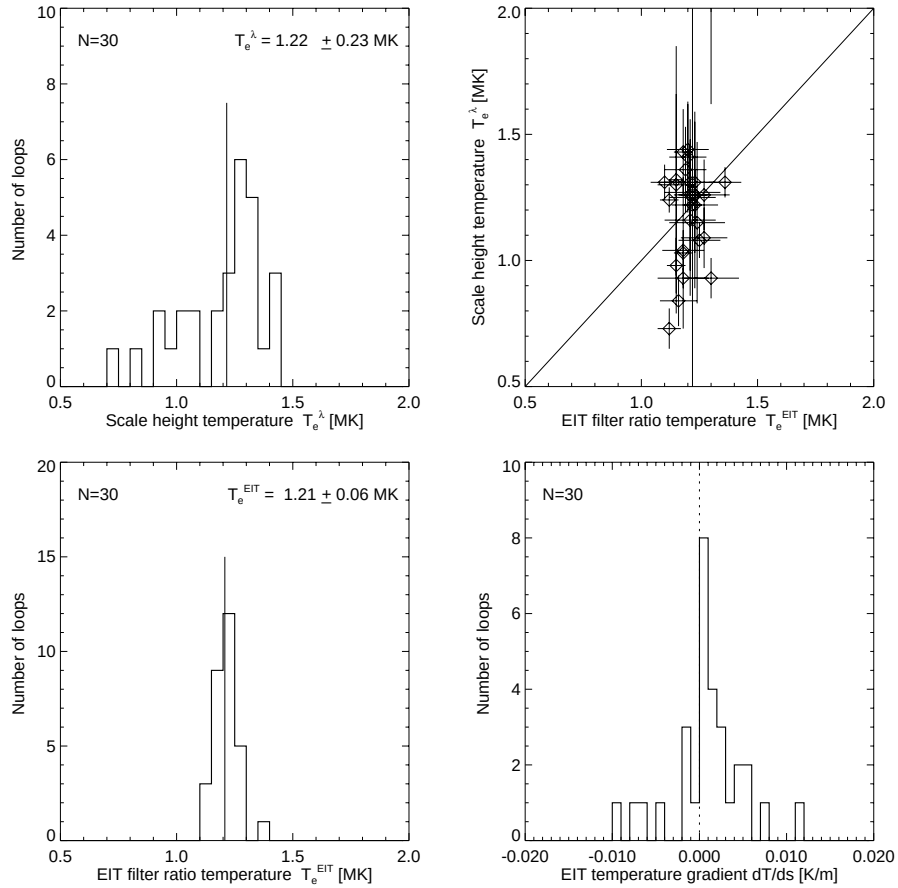

FIG. 11.—Statistics of scale height temperatures T_e^{λ} (*left top*), EIT filter-ratio temperatures $T_e^{\rm EIT}$ (*left bottom*), scatter plot of these two temperatures (*right top*), and EIT temperature gradients dT/ds (*right bottom*) for all analyzed 30 loops.

Figure 10 (*right*). We note that the filter-ratio temperature varies sometimes discontinuously along the loop, e.g., there is a jump from $T_e = 1.35$ MK to $T_e = 1.1$ MK at $s = 70$ Mm in loop 1 (Fig. 10, *top right*), which may be caused by contamination from a hotter loop that is located almost parallel to loop 1 at $s < 70$ Mm (see cross sections in Fig. 6). Such confusion problems can only be identified in hindsight. Despite such confusion problems, there seems to be a trend of a positive temperature gradient $dT/ds > 0$ above the footpoint for most of the loops (Table 2). To estimate these average temperature gradients (without correcting for multiloop confusion) we performed a linear regression $T_e(s)$ for all loops. The most significant temperature gradients are found for loop 11 ($dT/ds = +0.0049$ K m^{-1}), for loop 20 ($dT/ds = +0.0012$ K m^{-1}), and for loop 25 ($dT/ds = +0.0054$ K m^{-1}); see examples in Figure 10 and Table 1. The distribution of temperature gradients $N(dT/ds)$ is shown in Figure 11 (*bottom right*), revealing that $\approx 75\%$ of the loops have a positive temperature gradient $dT/ds > 0$ across the first scale height above their footpoints. Higher parts ($h \gtrsim 1\lambda$) of these loops are not detectable in EIT images due to insufficient density contrast (1 scale height corresponds to a factor of ≈ 3 in density or a factor of ≈ 10 in emission measure or EIT flux).

2.9. *Magnetic Field, Plasma-β Parameter, and Alfvén Velocity*

There is no accurate method available yet to determine the height dependence of the coronal magnetic field, nor to trace the magnetic field along a particular active region loop. Some attempts are in progress to match loop geometries observed in SXR or EUV with potential field models (constrained by the photospheric boundary and projections of coronal loops; Gary 1997; Gary & Alexander 1999). As a first approximation to investigate the magnetic field along the observed EUV loops, we calculate here a potential field model of AR 7986, using the code of Sakurai (1982) applied to a *SOHO*/Michelson-Doppler Imager (MDI) magnetogram, recorded on the same day as the EIT image (with a time difference of 20 hr). The potential field model is shown in Figure 12, overlaid on the MDI magnetogram, and coaligned with the traced EIT loops (by transforming the three-dimensional field lines according to the solar rotation rate during the time difference). Note that the EUV loops represent independent tracers of the plasma along magnetic field lines and thus convey an important test of how well the coronal magnetic field is represented with a potential field model. The match of the traced EUV loops with the potential field shown in Figure 12 is remarkably good, given the time difference of 20 hr and the nonpotential structure implied by currents that are likely to be present in this active region, imposed by the observed filament along the neutral line. Detailed modeling with potential and force-free magnetic fields and investigating the best match with individual loops traced from EIT and SXT images will be pursued in a subsequent study.

To estimate the magnetic field along the traced EIT loops we localize those potential field lines that have the closest

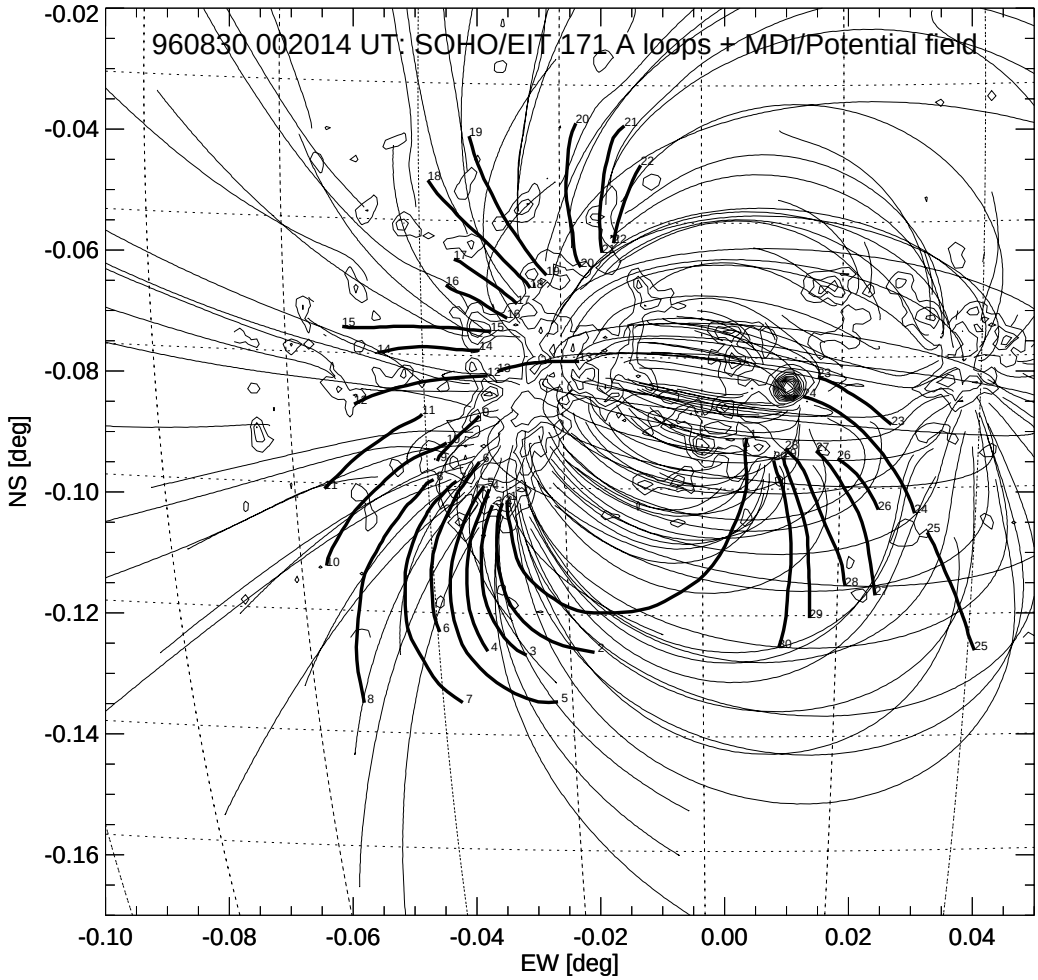

FIG. 12.—*SOHO*/MDI magnetogram recorded on 1996 August 30, 2048 UT, rotated to the time of the analyzed EIT image (1996 August 30, 0020:14 UT), with contour levels at $B = -350, -250, \ldots, +1150$ G (in steps of 100 G). Magnetic field lines calculated from a potential field model are overlaid (*thin lines*) onto the 30 loops (*thick lines*) traced from the *SOHO*/EIT image.

footpoints to the EIT loop footpoints and take the height dependence of their magnetic field strength $B(h)$ as a proxy for the EIT loops. The height dependence of the magnetic field $B(h)$ of the 30 potential field lines closest to the analyzed EIT loops is shown in Figure 13 (*top*). It can be approximated with a dipole model,

$$B(h) = B_{\rm foot}\left(1 + \frac{h}{h_D}\right)^{-3}, \qquad (7)$$

with a mean dipole depth of $h_D = 75$ Mm and a range of footpoint field strengths $B_{\rm foot} \approx 20, \ldots, 230$ G (dashed lines in Fig. 13, *top*), or a mean of $B_{\rm foot} \approx 100$ G.

With the potential field $B(h)$ and the measured density $n_e(h)$ and temperature profiles $T_e(h)$ we can now determine the height dependence of the plasma-β parameter for each of the 30 analyzed loops,

$$\beta(h) = \frac{n(h)kT_e(h)}{[B(h)^2/8\pi]} \approx 3.47 \times 10^{-15}\,\frac{n_e(h)T_e(h)}{B(h)^2}, \qquad (8)$$

which quantifies the ratio of the thermal to the magnetic pressure and thus provides a crucial criterion for magnetic confinement. The plasma-β parameter is shown in Figure 13 (*middle*), ranging typically at $\beta \lesssim 0.1$ in the entire coronal range ($h \lesssim 200$ Mm) of the EUV loops. We find only 2 (out of 30 loops) that exceed the critical limit of $\beta \geq 1$, possibly implying currents and nonpotential magnetic fields along the loops. Gary & Alexander (1999) found such regimes with $\beta \gtrsim 1$ in the upper corona at $h \gtrsim 0.2\,R_\odot$ from analysis of SXR loops, in contrast to the common belief that the coronal value is always $\beta \ll 1$ (Dulk & McLean 1978; Priest 1981; Sakurai 1989; Gary 1990; McClymont, Jiao, & Mikić 1997). Reliable measurements of the plasma-β parameter require fully resolved structures, such as single loops analyzed here (save for unknown filling factors), whereas line-of-sight averaged densities are expected to underestimate the density in loop structures and thus are biased toward too low β values.

A further plasma parameter that is of interest for coronal loop dynamics is the Alfvén velocity, which can be computed along individual loops thanks to the knowledge of the magnetic field $B(h)$ and density $n_e(h)$,

$$v_{\rm A}(h) = \frac{B(h)}{\sqrt{4\pi n_i(h) m_i}} \approx 2.18 \times 10^{11}\,\frac{B(h)}{\sqrt{n_e(h)}}\ {\rm cm\ s^{-1}}. \qquad (9)$$

This quantity is shown in Figure 13 (*bottom*). The Alfvén velocity is found to be highest near the footpoints of the analyzed EUV loops, ranging from $v_{\rm A}(h = 0) \approx 2000$ to 6000 km s^{-1}, and is dropping off steadily with larger height

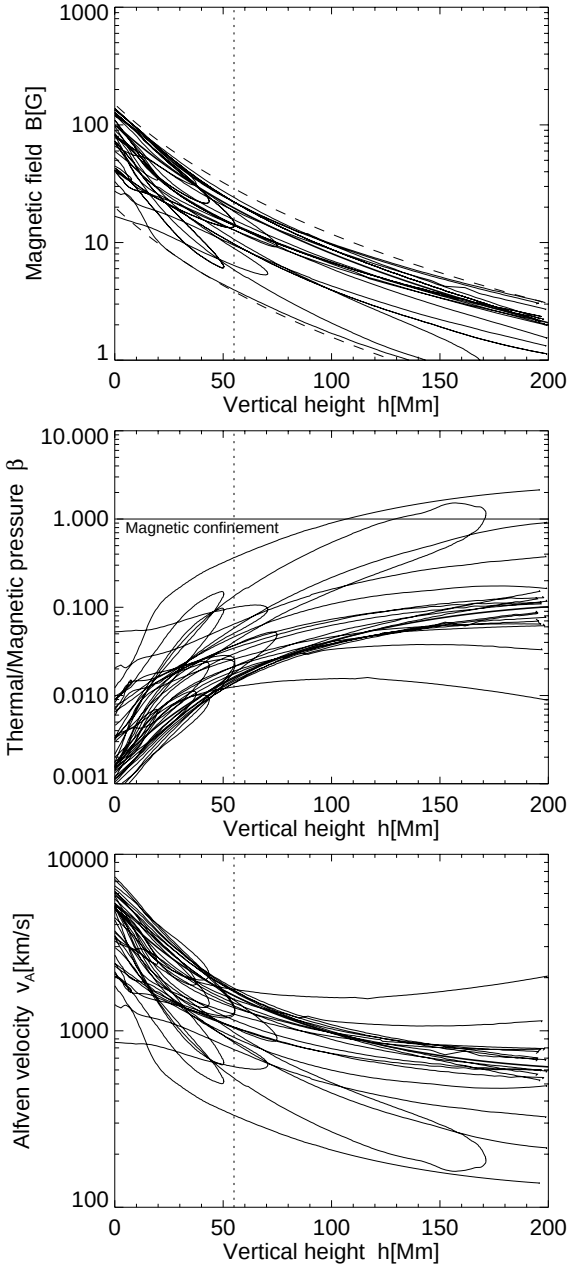

FIG. 13.—Magnetic field $B(h)$ (*top*), the plasma-β parameter or ratio of thermal to magnetic pressure, $\beta(h)$ (*middle*), and the Alfvén velocity $v_A(h)$ (*bottom*) determined as a function of height h for the 30 analyzed EIT loops. The magnetic field $B(h)$ is taken from the nearest potential field line (see Fig. 12). The vertical density scale height $\lambda = 55$ Mm is marked with a dotted line. A potential field model is indicated with dashed curves (*top*).

to a characteristic value of $v_A(h \gtrsim 100 \text{ Mm}) \approx 500$–$1000$ km s^{-1}.

3. PHYSICAL MODELS AND DISCUSSION

The density and temperature diagnostics obtained as functions of three-dimensional space coordinates allow us to investigate the physical conditions in the analyzed loops and to test some theoretical loop models and scaling laws. The major benefit of this study is that the loop geometry is well determined by the data, so that no geometric assumptions have to be made in the application of theoretical loop models.

3.1. *Loop Length Parametrization*

Because the thermal energy is generally much smaller than the magnetic energy in the corona [plasma parameter $\beta = n_e k_B T_e/(B^2/8\pi) \ll 1$], energy transport in coronal loops can be reduced to one dimension, as a function of the loop length parameter s. In our analysis we detected, except for one complete loop, only segments of loops that extend about 1 scale height above the primary footpoint. We will denote the start of the traced loop segments at the primary footpoint with $s = 0$, the end of the traced loop segment with $s = L_1$, and the full loop length extending all the way to the secondary footpoint with $s = L$. By localizing the secondary footpoint of traced loops from the global dipolar magnetic field of the active region, we obtained the approximate azimuth angle and length of the footpoint baseline. Using the stereoscopically determined inclination angle ϑ and the azimuth angle α of the footpoint baseline (Fig. 2), we were able to project the three-dimensional loop coordinates into the loop plane X-Z (eq. [A5]). In this loop plane we can approximate the loop geometry with a circular function, by interpolating the three loop positions ($s = 0, L_1, L$) with the circle parametrization [$X(\varphi)$, $Y(\varphi)$],

$$X = R_0 \cos \varphi \,, \tag{10}$$

$$Z = R_0 \sin \varphi + Z_0 \,, \tag{11}$$

yielding the circular loop radius R_0 and the offset Z_0 of the circle center from the footpoint baseline. The loop length $s(\varphi)$ can now be parametrized as a function of the circular angle φ,

$$s(\varphi) = R_0(\varphi + \varphi_0) \,, \quad -\varphi_0 \le \varphi \le (\pi + \varphi_0) \,, \tag{12}$$

where the starting angle φ_0 is defined by the loop radius R_0 and center offset Z_0,

$$\varphi_0 = \arcsin \frac{Z_0}{R_0} \,. \tag{13}$$

The full loop length L is then

$$L = R_0(\pi + 2\varphi_0) \,. \tag{14}$$

The geometric elements R_0, Z_0, L_1, and L are listed in Table 1 for all 30 loops. The same circular geometry was also used to visualize the extrapolated loop segments in Figure 5.

For the application of the hydrostatic equilibrium equation we need also to quantify the height dependence $h(s)$ of the loop length, which is determined by the loop plane inclination angle ϑ and equations (11)–(12),

$$h(s) = Z \cos \vartheta = \left[Z_0 + R_0 \sin \left(\frac{s}{R_0} - \varphi_0 \right) \right] \cos \vartheta \,. \tag{15}$$

The apexes or loop tops, $h_{\rm top} = (Z_0 + R_0) \cos \vartheta$, have a range of $h_{\rm top} = 30$–225 Mm in our sample of 30 loops and thus extend up to 4 scale heights (with $\lambda = 55 \pm 10$ Mm).

3.2. *Static Loop Model*

In static loop models it is assumed that mass flows can be neglected, leading to the basic steady state energy balance equation, e.g., derived by Rosner et al. (1978),

$$E_H(s) + E_R(s) - \nabla F_C(s) = 0 \,, \tag{16}$$

where E_H denotes the rate of heat deposition, E_R the energy radiated from the loop, and F_C is the thermal conductive flux, to be balanced at each location s of the loop in a static model.

The conductive flux term can be expressed in one-dimensional form (with the Spitzer thermal conductivity $\kappa = 0.92 \times 10^{-6}$ ergs s^{-1} cm^{-1} K$^{-7/2}$; Spitzer 1962, p. 144) by

$$\nabla F_C(s) = \frac{d}{ds}\left[-\kappa T^{5/2}(s)\frac{dT(s)}{ds}\right] \approx -\frac{5}{2}\kappa T^{3/2}(s)\left[\frac{dT(s)}{ds}\right]^2 \text{ ergs cm}^{-3}\text{ s}^{-1}, \quad (17)$$

where the approximation on the right-hand side includes only the linearized temperature dependence $T(s)$. The linearized temperature dependence can be written in terms of our measured temperature gradients (dT/ds) and mean temperatures $T_e^{\rm EIT}$ listed in Table 2 by

$$T(s) = T_e^{\rm EIT} + \left(\frac{dT}{ds}\right)\left(s - \frac{L_1}{2}\right). \quad (18)$$

The conductive flux term $\nabla F_C(s)$ in the energy balance equation (17) is calculated for $s = 0$ in Table 2, having a mean of $\langle \nabla(F_c)\rangle = (-0.003 \pm 0.005) \times 10^{-3}$ ergs cm^{-3} s^{-1}.

The radiative loss term $E_R(s)$ can be written in terms of the electron density $n_e(s)$ and the radiative loss function $\Lambda(T)$,

$$E_R(s) = -n_e(s)^2\Lambda[T(s)] \text{ ergs cm}^{-3}\text{ s}^{-1}, \quad (19)$$

which can be approximated with a constant value in our relatively narrow temperature range of interest ($T_e =$ 0.5–2.0 MK),

$$\Lambda[T] = 10^{-21.94} \text{ ergs cm}^{-3}\text{ s}^{-1} \quad (10^{5.75} < T < 10^{6.3}), \quad (20)$$

as calculated by Raymond, Cox, & Smith (1976) for solar abundances (Rosner et al. 1978; Fig. 10; and eq. [A1]). The radiative loss rate $E_R(s)$ is calculated for $s = 0$ in Table 2, having a mean of $\langle E_R\rangle = (-0.46 \pm 0.29) \times 10^{-3}$ ergs cm^{-3} s^{-1} for our 30 analyzed loops, surpassing the conductive loss rate by about 2 orders of magnitude (under the assumption of a filling factor of unity).

Static hydrodynamic loop models assume steady state conditions, i.e., the heating rate has to balance the energy losses by conduction and radiation according to equation (16). Because we find here that the conductive loss rate is much smaller than the radiative loss for this set of analyzed EUV loops, the required steady state heating rate has to balance essentially the radiative loss rate, i.e., $E_H \approx -E_R$. This steady state heating rate requirement E_H (defined by eq. [16]) is listed in Table 2, having a mean of $\langle E_H\rangle = (+0.46 \pm 0.28) \times 10^{-3}$ ergs cm^{-3} s^{-1}. Because the radiative loss rate is proportional to the squared density (eq. [19]), for which we found an exponential decrease with height (eq. [5]), the steady state heating rate requirement follows a similar exponential relation,

$$E_H(s) \approx -E_R(s) \approx n_{e0}^2\,\Lambda(T)\exp\left[-\frac{2h}{\lambda(T)}\right], \quad (21)$$

with an exponential scale height that equals half the density scale height. Such an exponential heating scale height s_H, or heat-deposition length, has been introduced, for instance in loop models of Serio et al. (1981),

$$E_H(s) = E_{H0}\exp\left(-\frac{s}{s_H}\right), \quad (22)$$

which has a mean value of $s_H = \lambda/2 = (55 \pm 10 \text{ Mm})/2 = 28 \pm 5$ Mm (see Table 1) for our group of EUV loops. This is a very stringent requirement for the spatial distribution of the heating function. It is very unlikely that the heating function always adjusts to the gravitational stratification without thermal conduction. However, because we found that conductive loss is 2 orders of magnitude smaller than radiative loss, the observed temperature and density structure of EUV loops can only be controlled by a combination of heating and radiative loss. Because these two terms cannot be balanced in a natural way, we conclude that the observed EUV loops *are not in steady state* and thus cannot be explained with static models.

Coronal loops in steady state conditions have also been simulated numerically, where solutions of the static energy equation yield the result that the conductive energy loss is about equivalent to twice the radiative loss (e.g., Vesecky, Antiochos, & Underwood 1979). Consequently, for loops in steady state condition, the heating rate, the conductive loss, and the radiative loss are all of about the same order. The fact that we find the conductive loss to be 2 orders of magnitude smaller than radiative loss violates this rule of thumb for steady state condition. Therefore, we conclude that the observed EUV loops are not in steady state condition but rather in a cooling phase, far off the equilibrium.

3.3. *Loop Lifetime*

To investigate the lifetime of loops we have to consider the fastest of the energy loss timescales. The conductive loss time,

$$\tau_{\rm cond} = \frac{E_{\rm th}}{dE_C/dt} = \frac{3n_e k_b T_e}{\nabla F_C} \approx 1.1 \times 10^{-9} n_e T^{-5/2} L_0^2 \text{ [s]}, \quad (23)$$

is found to be $\tau_{\rm cond} \approx 9 \times 10^5$ s (or 10 days), using the average parameters from Table 1, $n_e = 1.92 \times 10^9$ cm^{-3}, $T_e^{\rm EIT} = 1.22 \times 10^6$ K, and $L_0 = L/2 = 2.2 \times 10^{10}$ cm. The conductive loss time of EUV loops is therefore substantially longer than for SXR loops, for two reasons (1) the temperature is cooler, and (2) the loop length is somewhat larger. If we compare typical SXR loops as observed with *Yohkoh*/SXT, where typical temperatures of $T_e^{\rm SXR} = 5$ MK, densities of $n_e = 3 \times 10^9$ cm^{-3}, and loop lengths of $L^{\rm SXR} = 10^{10}$ cm were measured (Kano & Tsuneta 1995), we find conductive loss times of $\tau_{\rm cond}^{\rm SXR} \approx 8 \times 10^3$ s (or 2.4 hr). The huge difference in the conductive loss times of EUV and SXR loops comes mainly from the temperature factor, $(T^{\rm SXR}/T^{\rm EUV}) \approx 5$, which raised to the $T^{-5/2}$ power yields a ratio of

$$\frac{\tau_{\rm cond}^{\rm EUV}}{\tau_{\rm cond}^{\rm SXR}} \approx \left(\frac{T^{\rm EUV}}{T^{\rm SXR}}\right)^{-5/2} \approx 55, \quad (24)$$

i.e., the conductive loss time is about 55 times longer for EUV loops than for SXR loops.

Let us now estimate the radiative loss time of EUV loops (under the assumption of a filling factor of unity). The radi-

ative lifetime is

$$\tau_{\rm rad} = \frac{E_{\rm th}}{dE_R/dt} = \frac{3n_e k_b T_e}{n_e^2 \Lambda(T_e)}, \quad (25)$$

yielding a mean lifetime of $\tau_{\rm rad} \approx 2.3 \times 10^3$ s or about 40 minutes, based on our mean values $\langle n_e \rangle = 1.92 \times 10^9$ cm^{-3}, $\langle T_e \rangle = 1.22$ MK, and $\Lambda(T) = 10^{-21.94}$ ergs cm^{-3} s^{-1}. Comparing the radiative lifetime of EUV loops with SXR loops, there is less of a difference than for the conductive loss time. This similarity is because the mean electron densities are comparable, i.e., $n_e^{\rm EUV} \approx 2 \times 10^9$ cm^{-3} versus $n_e^{\rm SXR} \approx 3 \times 10^9$ cm^{-3} (Kano & Tsuneta 1995), and the radiative loss function has only a slightly smaller value at SXR temperatures, i.e., $\Lambda(T^{\rm EUV}) \approx 10^{-21.94}$ ergs cm^{-3} s^{-1} (eq. [17]) versus $\Lambda(T^{\rm SXR}) \approx 10^{-22.18}$ ergs cm^{-3} s^{-1} (Kano & Tsuneta 1995), whereas the temperatures differ by a linear factor $T^{\rm SXR}/T^{\rm EUV} \approx 5$. The ratio of radiative loss times between EUV and SXR loops is therefore mainly determined by the temperature ratio,

$$\frac{\tau_{\rm rad}^{\rm EUV}}{\tau_{\rm rad}^{\rm SXR}} \approx \left(\frac{T^{\rm EUV}}{T^{\rm SXR}}\right) \approx 0.2, \quad (26)$$

yielding a radiative cooling time of $\tau_{\rm rad}^{\rm SXR} \approx 10^4$ s (or about 3 hr) for SXR loops. The mean physical loop parameters of EUV and SXR loops and the resulting timescales are also summarized in Table 3 for convenience.

From these average physical parameters of our 30 analyzed EIT loops we find therefore that the conductive cooling time is at least 2 orders of magnitude larger than the radiative cooling time, a result that we have already noticed by comparing conductive loss rates versus the radiative loss rates in Table 2. This extreme ratio for EUV loops is in marked contrast to SXR loops, where the ratio $\tau_{\rm cond}^{\rm SXR}/\tau_{\rm rad}^{\rm SXR} = 8 \times 10^3/10^4 \approx 1$ is close to unity if we use the mean loop parameters of Kano & Tsuneta (1995). An even greater difference was found by Porter & Klimchuk (1995) and Priest et al. (1998), who measured ratios $\ll 1$ for individual SXR loops. Note that, for many of these loops, the ratio may actually be near unity if we allow for the possibility of small filling factors (see § 3.5). It is therefore possible that a majority of SXR loops are in quasi-static equilibrium. This is definitely not the case for the EUV loops, since small filling factors make the discrepancy between the radiative and conductive loss rates even larger. The ratio of conductive to radiative cooling times of EUV loops is even more different with respect to large-scale SXR loops, where the opposite ratio was found, i.e., the conductive loss being 2 orders of magnitude stronger than radiative loss (Priest et al. 1998).

We have only limited information on the real lifetime of the analyzed loops. A lower limit is constrained by the radiative cooling time, amounting to 40 minutes at the loop base. The real lifetime can be a few times longer, if radiative cooling is partially balanced by heating. However, the real lifetime cannot be much longer than the radiative cooling time because the required heating function would then have to be extremely fine tuned close to the steady state condition, which is implausible without the effect of thermal conduction. Based on this argument we conclude that the real lifetime cannot exceed a few radiative cooling times, say a few hours. This conclusion is somewhat supported by the localization capability of our dynamic stereoscopy method. The stereoscopic correlation over time intervals of ± 24 hr clearly shows spatial displacements of loops. It is therefore conceivable that the heating function is not cospatial over 24 hr, but rather spreads over multiple neighbored field lines, where individual loop strands cool off on timescales as short as the radiative cooling time ($\approx$40 minutes). Short-term fluctuations in $T_e \lesssim 1.0$ MK on the order of 5–10 minutes were also reported by Habbal, Ronan, & Withbroe (1985). A conceivable scenario is quasi-periodic microflare heating as simulated by Peres (1997).

3.4. *Loop Scaling Laws*

Scaling laws have been derived among physical loop parameters (such as the temperature T_e, the loop pressure p, the loop length L, the steady state heating rate requirement E_H [in a steady state model], and the magnetic field B), to test the internal self-consistency of the energy balance equation for a given set of observed loops. We show the relationships between these parameters in the form of correlation plots for our sample of 30 EUV loops in Figure 14, including the loop length L, the loop base pressure $p_0 = p(h = 0)$, the steady state heating rate at the footpoint $E_{H0} = E_H(h = 0)$, and the magnetic field $B_{\rm foot}$ at the footpoint. The footpoint field strengths $B_{\rm foot}$ have been measured from the MDI magnetogram by taking the maximum field values among the nearest MDI pixels to the EIT loop footpoints (see values of $B_{\rm foot}$ listed in Table 2).[3] We omit correlations with the temperature because this parameter is almost constant ($T_e^{\rm EIT} = 1.21 \pm 0.06$) for our data set. Linear regres-

[3] The cautious reader may make a distinction between a photospheric and coronal footpoint definition, which can be related using flux conservation as $\langle B_{\rm cor} \rangle r_{\rm cor}^2 = \langle B_{\rm phot} \rangle r_{\rm phot}^2$, in case of a canopy-like divergence from photospheric flux tube radius $r_{\rm phot}$ to coronal footpoint radius $r_{\rm cor}$. This effect is not considered here.

TABLE 3

COMPARISON OF MEAN PHYSICAL LOOP PARAMETERS IN EUV AND SXR

Parameter	EUV (This Work)	SXR (Kano & Tsuneta 1995, 1996)
Objects	*Cool* loops	*Hot* loops
Observations	*SOHO*/EIT 171 Å	*Yohkoh*/SXT
Electron temperature T_e (MK)	1.2	5
Electron density n_{e0} (cm^{-3})	2×10^9	3×10^9
Loop half-length L (cm)	2×10^{10}	1×10^{10}
Loop pressure p_0 (dyne cm^{-2})	0.6	4
Conductive loss time $\tau_{\rm cond}$ (s)	9×10^5	8×10^3
Radiative loss time $\tau_{\rm rad}$ (s)	2×10^3	1×10^4
Ratio $\tau_{\rm cond}/\tau_{\rm rad}$	450	1

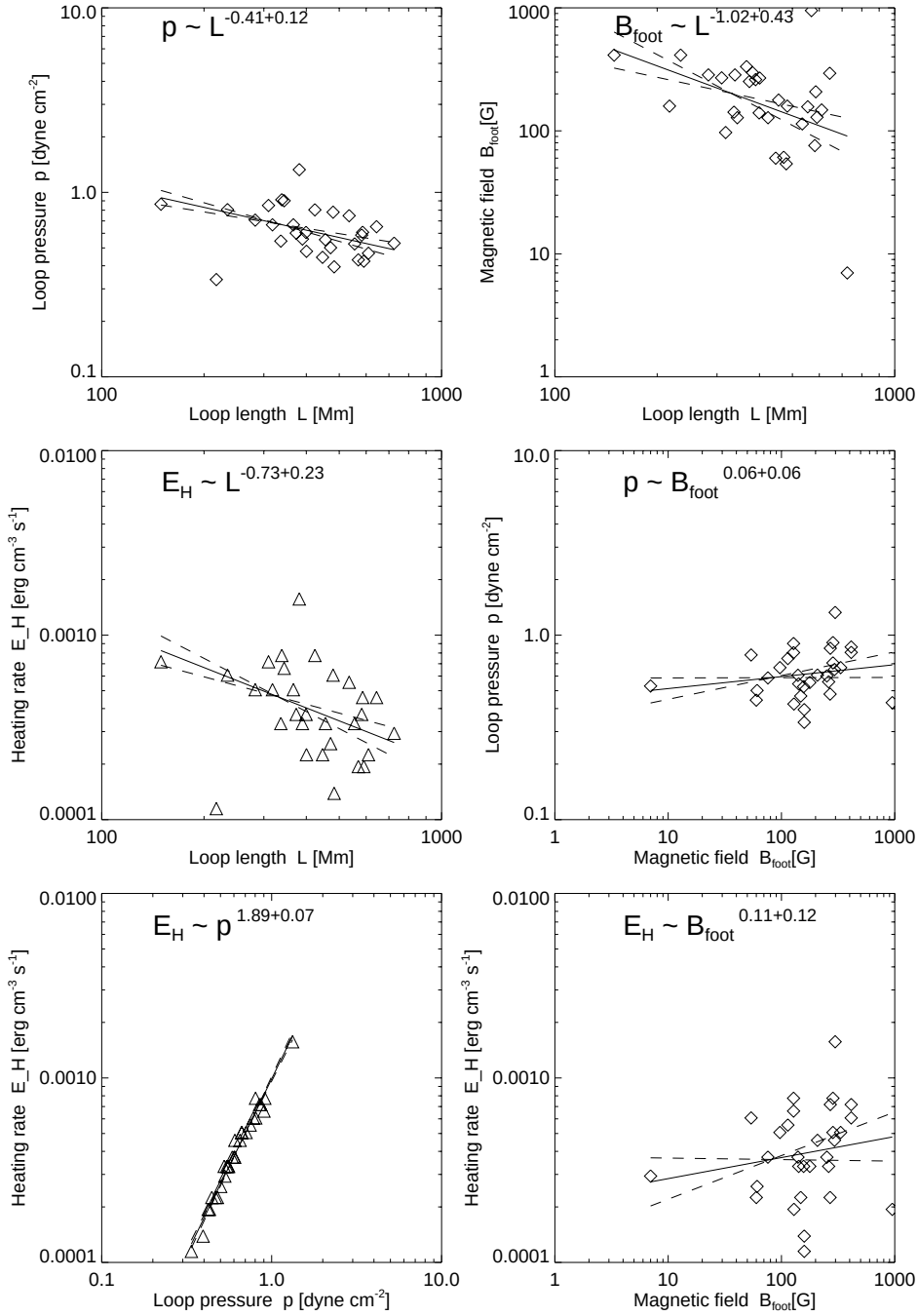

FIG. 14.—Scaling laws between the steady state heating rate requirement E_{H0}, loop base pressure p_0, loop length L, and magnetic field strength $B_{\rm foot}$ for our sample of 30 EUV loops. Linear regression fits are indicated with solid lines, the standard deviations of the slopes are marked with dashed lines.

sion fits reveal the following correlations

$$p_0 \propto L^{-0.41\pm0.12}\,, \tag{27}$$

$$B \propto L^{-1.02\pm0.43}\,, \tag{28}$$

$$E_{H0} \propto L^{-0.73\pm0.23}\,, \tag{29}$$

$$E_{H0} \propto p_0^{1.89\pm0.07}\,. \tag{30}$$

We do not find a significant correlation between the loop pressure p_0 and the magnetic field $B_{\rm foot}$ (Fig. 14, *middle right*), or between the heating rate E_{H0} and the magnetic field $B_{\rm foot}$ (Fig. 14, *bottom right*).

First, let us discuss the scaling between loop pressure and loop length. From the analysis of SXR loops (Porter & Klimchuk 1995; Klimchuk & Porter 1995), a power-law index of $-1.82 \le \beta \le -0.22$ (90% confidence range) was found for the correlation $p_0 \propto L^{\beta}$. This result is consistent with our findings from EUV loops, with $\beta = -0.41 \pm 0.12$ (1 σ standard deviation, eq. [27]). The theoretical interpretation of this value β depends on the heating deposition length in the context of a specific heating model. In the simplest case where the heating source is localized in a point source and does not depend on any other physical parameters, i.e., the same amount of thermal energy is deposited in loops of different lengths, the volumetric heating rate would scale as $E_H \propto L^{-1}$. If we additionally assume that the heating rate has to balance the radiative loss, $E_H \propto p^2$, as supported by the observed correlation (eq. [30]), then the pressure is expected to scale with loop length by $p_0 \propto L^{-0.5}$,

or $\beta = -0.5$, for one-dimensional loops. This is consistent with our observed relation $p_0 \propto L^{-0.41 \pm 0.21}$ (eq. [27]).

Second, we discuss the physical interpretation of correlations with the heating rate E_{H0}. Inserting the definition of the loop base pressure p_0,

$$p_0 = p(h = 0) = 2n_{e0} k_B T_e^{\rm EIT} , \quad (31)$$

into the steady state heating rate E_H that is required to balance the dominant radiative loss $-E_R$ (eq. [21]), we find immediately

$$E_{H0} \propto n_{e0}^2 \approx p_0^2 , \quad (32)$$

since the temperature $T_e^{\rm EIT}$, as well as the radiative loss function $\Lambda(T)$, can be approximated by a constant for the given data set. This explains, by definition, the correlation found for EUV loops (eq. [30]). Such a dependence ($E_{H0} \propto p^2$) was also inferred for soft X-ray bright points (Kankelborg, Walker, & Hoover 1997). Note that this scaling law is distinctly different from that derived by Rosner et al. (1978), or Galeev et al. (1981),

$$E_{H0} \approx 10^5 p_0^{7/6} L_0^{-5/6} , \quad (33)$$

which was derived under the assumption of quasi-static equilibrium, in which radiative and conductive losses are necessarily comparable (e.g., Vesecky et al. 1979). The same applies to the generalized scaling law of Serio et al. (1981), who account for a nonconstant pressure $p(h)$, parametrized by a pressure scale height s_p and a heading deposition scale height s_H,

$$E_{H0} \approx 10^5 p_0^{7/6} L_0^{-5/6} \exp\left[0.5L\left(\frac{1}{s_H} - \frac{1}{s_p}\right)\right] . \quad (34)$$

Also Kano & Tsuneta (1996) derived an energy scaling law by equating radiative and conductive energy loss, for the special case of the heating source is located at the loop top,

$$E_{H0} = 4.0 \times 10^3 (p_0 T_m^{1/2}) L_0 \text{ ergs cm}^{-3} \text{ s}^{-1} \quad (35)$$

with T_m the maximum temperature at the loop top. Similarly, Ofman, Klimchuk, & Davila (1998) derive a heating rate scaling law for resonant absorption of Alfvén waves under the assumption of quasi steady state equilibrium. Consequently, because all these energy scaling laws are based on the assumption of quasi-static equilibrium, in which radiative and conductive losses are necessarily comparable, they are not applicable to our set of EIT loops, where conductive loss is completely negligible compared with the radiative loss.

Third, we discuss the physical meaning of correlations with the magnetic field. For models where loop heating is accomplished by dissipation of magnetic energy (e.g., nanoflare heating model of Parker 1988), one would expect a relation $E_H \propto B^2$, which is not consistent with our findings because we did not find any significant correlation between E_H and $B_{\rm foot}$ (Fig. 14, *bottom right*). In many coronal heating models, the dissipated energy E_H depends also on the loop length L. It is then useful to investigate the specific dependence of the magnetic field B on the loop length L from observations, e.g., specified by a power law (Porter & Klimchuk 1995),

$$B \propto L^{\delta} . \quad (36)$$

Theoretically, a power-law index of $\delta = -3$ is expected for a point dipole, or $\delta = -2$ for a line dipole, in the far-field approximation. In the near field, i.e., for field lines comparable with the dipole separation, these relations are strongly modified (approaching a regime of $\delta \approx 0$). The distinction between the near-field and far-field approximations should therefore be taken into account in the application of a $B(L)$ relation. Klimchuk & Porter (1995) inferred that $\delta \approx -0.7$ by combining their $P \propto L^{-1}$ result for SXR loops with the *Skylab* result of Golub et al. (1980) that $P_{\rm AR} \propto B_{\rm AR}^{1.6}$, where the subscripts refer to averages over entire active regions. Recent work with more detailed magnetic field modeling yields a value of $\delta = -0.97 \pm 0.25$ (Mandrini, Demoulin, & Klimchuk 1999). This recent value obtained from magnetic field extrapolations of many active regions agrees very well with the value found here from EUV loops, $\delta \approx -1.02 \pm 0.42$ (eq. [28]). The value of $\delta \approx -1$ for both SXR and EUV loops indicates that the observed loops belong to the near-field regime rather than to the far-field case. Interestingly, no correlation was found between $B_{\rm foot}$ and L for large-scale magnetic fields of the global corona, which extends out to the heliosphere (Wang et al. 1997).

3.5. *Loop Filling Factors*

So far we assumed a filling factor of unity in our derivation of physical loop parameters. However, there is some indirect evidence that coronal loops may consist of many unresolved thin strands (Golub et al. 1990), which suggests a higher electron density inside the strands than obtained from the volume-averaged emission measure across a macroscopic loop diameter. If we denote the true density inside the strands with n_e^* and the volume filling factor of strands by f, the two densities relate by

$$n_e^*(s) = \sqrt{\frac{\text{EM}(s)}{w_z(s)} \frac{1}{f}} = \frac{n_e(s)}{\sqrt{f}} . \quad (37)$$

This filling factor affects the radiative loss rate (eq. [19]), but not the conductive loss rate (eq. [17]). Numerical solutions of the static energy equation in coronal loops have shown that the conductive energy loss to the chromosphere is about twice as much as the radiative loss in the corona (Vesecky et al. 1979). Based on this argument, the filling factor can be derived by equating twice the conductive loss rate with the radiative loss rate, $2\nabla F_C(s) \approx E_R(s)$. Porter & Klimchuk (1995) used this approach to infer filling factors $\ll 1$ for most of the 47 SXR loops they analyzed. Several had filling factors greater than 1, an unphysical situation that led them to conclude that those particular loops cannot be in quasi-static equilibrium. We find a similar situation for our EUV loops. Introducing a filling factor less than 1 would increase the radiative loss rate, but not the conductive loss rate, and so the 2 order of magnitude discrepancy that already exists would become even larger. Thus, our conclusion that the loops are not in equilibrium seems inescapable. It is interesting to note that the nonequilibrium loops of the Porter and Klimchuk study are relatively cool at $T \approx 2$ MK. They may belong to a separate class of loops (Cargill & Klimchuk 1997) that includes the EIT loops presented here.

3.6. *Hydrostatic Equilibrium*

The exponential density profiles $n_e(h)$ of our analyzed sample of EUV loops together with the finding that the resulting scale height temperature ($T^{\lambda} = 1.22 \pm 0.23$ MK) matches exactly the filter-ratio temperature ($T^{\rm EIT} = 1.21 \pm 0.06$ MK) in the statistical average, clearly proves that these EUV loops are in hydrostatic equilibrium. On the

other hand we found that these EUV loops are not in steady state condition, but are dominated by radiative cooling. The question arises then how pressure changes due to unbalanced heating or cooling processes can always adjust to hydrostatic equilibrium. Pressure gradients propagate with sound speed,

$$v_s = \sqrt{\frac{\gamma k_B T_e}{\mu m_H}} \approx 1.51 \times 10^4 \sqrt{T_e} \text{ cm s}^{-1} , \quad (38)$$

which amounts to $v \approx 165$ km s^{-1} for the observed EUV loops with an average temperature of $T_e \approx 1.2$ MK. Based on the mean scale height of $\lambda = 55$ Mm, the sound travel time across a scale height is $t_s = \lambda/v_s = 330$ s, or about 5 minutes. Because this sound travel time is therefore always much shorter than the radiative cooling time, with a minimum value of $\tau_{\rm rad}^0 \approx 40$ minutes at the loop base, increasing to $\tau_{\rm rad}(h = \lambda) \approx 110$ minutes at a height of 1 scale height, pressure changes can always be adjusted to hydrostatic equilibrium, so that we expect these loops always to be close to hydrostatic equilibrium. This is also consistent with results based on numerical simulations of the thermal stability. Although uniform-pressure loops were found to be thermally unstable under some conditions (e.g., if the base heat flux is too small), the influence of gravity (or hydrostatic equilibrium) was found to have a stabilizing effect (Wragg & Priest 1982). These arguments may partially explain the numerous existence of hydrostatic EUV loops observed by EIT during four solar rotations in this active region.

3.7. *A Statistical Heating Model for EUV Loops*

Our measurements have shown two important findings: (1) EUV loops are in hydrostatic equilibrium, and (2) radiative energy loss dominates conductive loss completely. The second finding is in strong contrast to SXR loops, which are found to be close to steady state condition, where radiative cooling and thermal conduction are comparable. Consequently, EUV loops are far off the steady state equilibrium, and their temperature structure cannot be explained by steady state models. Although it is mathematically possible to construct a heating function that exactly balances the radiative loss (eq. [21]), the conductive loss rate cannot be increased (given the observed temperature gradients) to match the radiative loss, a necessary condition for static equilibrium. It is therefore more reasonable to invoke a model that does not require static equilibrium, e.g., a dynamic model with a time-dependent heating function.

Because thermal conduction is demonstratedly not essential in EUV loops, we cannot assume a single localized heating source, e.g., at the loop top, but rather have to assume a heating function that acts in all parts of the loop, either uniformly or randomly distributed, but affecting all parts of the loops in the temporal average. The loop can be subdivided into multiple strands, where the heating function acts randomly in different strands, or along the loop strands (Fig. 15, *top*). Let us characterize such a heating function with a fragmented topology, where each elementary heating event has a dissipation length l_h (Fig. 15, *top*) and occurs with a mean recurrence rate $R = 1/t_R$ at a given loop position h. The duration of the heating event has to be shorter than the local radiative cooling time $\tau_{\rm rad}$ because the loops would cool off faster than they can be heated otherwise. The radiative cooling time depends primarily on the

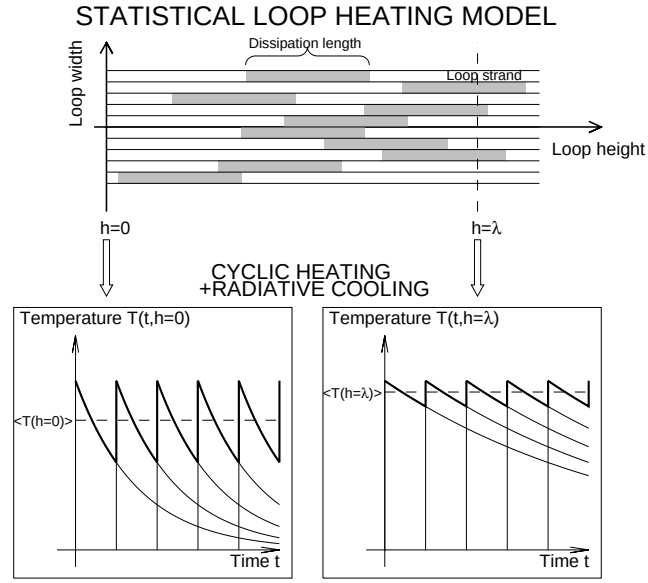

FIG. 15.—Cartoon of a statistical loop heating model, where heating events are uniformly or randomly distributed along and across a loop (possibly in different loop strands) and occur cyclically with a mean recurrence time. Because the heated loop portions cool off faster at the loop footpoints (due to the shorter radiative cooling time, *bottom left*) than in larger heights, i.e., at 1 scale height, $h = \lambda$ (*bottom right*), a positive temperature gradient arises in the statistical average.

density and has therefore a height dependence that is related to the hydrostatic equilibrium, i.e.,

$$\tau_{\rm rad}(h) = \frac{3 n_e(h) k_b T_e}{n_e(h)^2 \Lambda(T_e)} \approx \tau_{\rm rad}^0 \exp\left(\frac{h}{\lambda}\right), \quad (39)$$

where $\tau_{\rm rad}^0$ refers to the radiative cooling time at the loop base ($h = 0$). Since the heating timescale has to be shorter than the radiative cooling time, we can neglect it to first order and obtain a sawtooth-like temperature profile $T_e(t)$ for a recurrent sequence of heating events, i.e., the loop is heated cyclically to a temperature $T_{\rm max}$ and cools off with an exponential decay time $\tau_{\rm rad}$ (Fig. 15, *bottom*). Because the radiative cooling time increases with height due to the hydrostatic density dependence, the loops will cool off slower in larger heights and thus maintain a higher temperature in the temporal average. This simple model already explains the basic mean temperature structure of EUV loops, producing a positive temperature gradient with height (without invoking thermal conduction). We can now derive the mean loop temperature $\langle T_e(h) \rangle$ as a function of the height by averaging the time-dependent temperature evolution during one heating cycle t_R (the mean recurrence time of a heating event),

$$\langle T_e(h) \rangle = \frac{\int_0^{t_R} T_{\rm max} \exp\left[-t/\tau_{\rm rad}(h)\right] dt}{\int_0^{t_R} dt} = T_{\rm max} \left[\frac{\tau_{\rm rad}(h)}{t_R}\right] \left\{1 - \exp\left[-\frac{t_R}{\tau_{\rm rad}(h)}\right]\right\} . \quad (40)$$

Inserting the height dependence of the radiative cooling time $\tau_{\rm rad}(h)$ from equation (39) yields then the following temperature profile,

$$\langle T_e(h) \rangle = T_{\rm max} \frac{1}{q_R} \exp\left(\frac{h}{\lambda}\right) \left\{1 - \exp\left[-\frac{q_R}{\exp(h/\lambda)}\right]\right\} , \quad (41)$$

where we defined a dimensionless recurrence time ratio q_R by

$$q_R = \frac{t_R}{\tau_{\rm rad}^0} . \tag{42}$$

The average temperature gradient dT/dh over a scale height λ is then

$$\frac{dT}{dh} \approx \frac{T_e(h=\lambda) - T_e(h=0)}{\lambda} = \frac{T_{\rm max}}{\lambda} \frac{1}{q_R} \left\{ e\left[1 - \exp\left(-\frac{q_R}{e}\right)\right] - [1 - \exp(-q_R)] \right\} , \tag{43}$$

which can be related to the measured temperature gradients dT/ds described in § 2.8 (see also Table 2). We see that the temperature gradient depends only on one free model parameter, the recurrence time ratio q_R. For very short recurrence times, $q_R \ll 1$, the temperature gradient becomes zero because heating is almost continuous and thus maintains the loop temperature everywhere near $T_{\rm max}$ and is therefore constant along the loop. On the other side, the rarer the heating events, the more the loop will cool off before onset of the next heating event, and thus the steeper a temperature gradient will arise due to the hydrostatic dependence of the radiative cooling time. A comparison of the measured temperature gradient with this model allows therefore to constrain the recurrence time. We show the theoretical temperature profiles $\langle T_e(h) \rangle$ (eq. [41]) in Figure 16 (*left*), for a set of recurrence ratios $q_R = 0, \ldots, 1$, with the maximum temperature $T_{\rm max}$ adjusted for each case in such a way that the loop base has a temperature of $T_e(h=0) = 1.2$ MK, as observed for our set of EIT loops. The resulting temperature gradients $dT/dh(h=0)$ at the loop base are shown as a function of the recurrence time t_R in Figure 16 (*right*), where we find the following behavior: (1) the temperature gradient is very shallow ($dT/dh < 0.01$ K m^{-1}) for fast recurrence times ($t_R < t_{\rm rad}^0$), and (2) a maximum temperature gradient of $(dT/dh)_{\rm max} \lesssim 0.04$ K m^{-1} is predicted for long recurrence times. We mark the observed temperature gradients dT/ds in this diagram (crosses in Fig. 16, *right*), to infer the recurrence times that are consistent with the observations. We find that most of the EIT loops (20 out of 30) have temperature gradients that require recurrence time ratios of $q_R \lesssim 0.25$, or recurrence times of $t_R = q_R \times \tau_{\rm rad}^0 \lesssim 10$ minutes (based on $\tau_{\rm rad}^0 \approx 40$ minutes). From this model we predict that heating events should occur with a mean rate of about 5 minutes in a given loop location to maintain the observed temperature gradient in EUV loops. The predicted correlation between temperature gradients (dT/dh) and temperature fluctuation rates R could possibly be checked with high-cadence EIT movies (Newmark et al. 1997).

This heating model is entirely constrained by the observed temperature $T_e(s)$ and density profile $n_e(s)$ and predicts a recurrence rate R at a given loop location. In order to affect the entire length of a loop strand, the total rate R of heating events has to be multiplied by the ratio of the loop length L to the dissipation length $l_{\rm heat}$ of an individual heating event,

$$R_{\rm strand} = R \frac{L}{l_{\rm heat}} . \tag{44}$$

If the loop is composed of $N_{\rm strand}$ strands, the required total number $R_{\rm loop}$ of heating events scales with the ratio of strand cross sections to the loop cross section, i.e.,

$$R_{\rm loop} = R_{\rm strand} \left(\frac{w}{w_{\rm strand}}\right)^2 = R \frac{L}{l_{\rm heat}} \left(\frac{w}{w_{\rm strand}}\right)^2 , \tag{45}$$

where $w_{\rm strand}$ indicates the width of a strand. If the width of individual strands is very small, the total rate of heating events becomes so large that the variability of individual heating events cannot be resolved with currently available time cadences, and the temperature profile of the loop will appear smooth in space and time. Future investigations will reveal whether individual heating events can be resolved or not.

The purpose of this simple statistical heating model without conduction is just to illustrate that the observed temperature gradients can naturally be explained with recurrent heating events uniformly distributed all over the entire loop. A heating source that is confined to a small part of the loop cannot explain the temperature structure of EUV loops. For instance, a heating source localized at the loop-top cannot balance the radiative energy loss in the lower part of the loop (because thermal conduction is inefficient in EUV loops), an argument that was used by Neupert et al. (1998) against the heat-deposition model at large heights (e.g., Wheatland, Sturrock, & Acton 1997). A conductionless heating model necessarily requires a heating

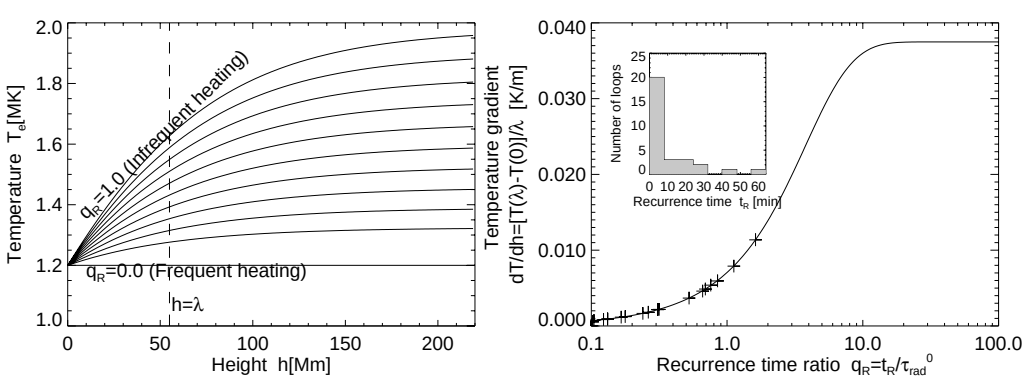

FIG. 16.—Temperature profiles $T_e(h)$ along a loop predicted by the statistical loop heating model (Fig. 15) are shown for different recurrence time ratios $q_R = 0, 0.1, 0.2, \ldots, 1.0$ (*left*). The resulting temperature gradients dT/dh are shown as a function of the recurrence time ratio q_R (*right*). The crosses mark the temperature gradients observed in the 30 EIT loops, and the resulting distribution of recurrence times t_R is shown in the form of a histogram (insert). Note that most of the required recurrence times are $\lesssim 10$ minutes.

function that covers the entire loop, either uniformly or randomly distributed (in space and time). Because a uniform heating function requires an implausible fine tuning with the hydrostatic equilibrium, we invoke a statistical heating function. At this point we leave it open whether the statistical heating events can be interpreted by nanoflares (Parker 1988), by resonant dissipation of Alfvén waves (Ofman et al. 1998), or by cyclically driven mass flows (e.g., chromospheric evaporation cycles, spicules, surges, jets, injections). A scenario with quasi-periodic microflare heating has been modeled, e.g., by Cargill (1994), Cargill & Klimchuk (1997), or Peres (1997). In the nanoflare concept, dominant radiation loss (with a ratio of $\tau_{\rm rad}/\tau_{\rm cond} \approx 10^{-2}$), as observed for the EIT loops here, would occur in the final cooling phase of a nanoflare event, according to a model of Cargill (1994).

3.8. *Mass Flows in EUV Loops*

In the discussion of heating requirements we neglected mass flows, which could play a significant role. Downflows were found from Doppler shift measurements at EUV temperatures of $T_e \approx 1$ MK that carry an energy flux comparable with radiative energy loss (Foukal 1978). Upflows with (Doppler shift) velocities of 50 km s^{-1} have been reported in Mg IX and Mg X lines ($T_e \approx 1$ MK) in an active region recently observed with *SOHO*/CDS (Brekke et al. 1997). Brown (1996) performed hydrodynamic simulations of loops that cool from an initial temperature of $T_e = 2$ MK down to temperatures of $T_e = 0.1$ MK, with subsequent heating back to the original temperatures of $T_e = 2$ MK (in cycles of 3000 s). These simulations demonstrate that downflows with velocities of 7–45 km s^{-1} occur during the cooling phase due to coronal condensation.

4. SUMMARY AND CONCLUSIONS

We developed a three-dimensional analysis method designed to determine geometric and physical parameters of loop structures in solar EUV or SXR images. This method, called dynamic stereoscopy, makes use of stereoscopic correlations of dynamically evolving loop structures that can be traced from high-pass filtered images. The method is designed to separate closely spaced, nested loops, in the plane of the sky, as well as along the line of sight, by suitable background subtraction. With this method we analyzed *SOHO*/EIT Fe IX, Fe X, and Fe XII observations of active region AR 7986, obtained on 1996 August 30. We traced 30 loop segments of this active region and determined the three-dimensional Cartesian space coordinates [$x(s)$, $y(s)$, $z(s)$], the loop widths $w(s)$, the electron density $n_e(s)$, and the electron temperature $T_e(s)$ as a function of the loop length s. The vertical density scale height λ of these loops was properly corrected for the inclination angle ϑ of the loop plane to the vertical, and the column depth $w_z(s)$ of loops was corrected for the projection angle $\psi(s)$ between the loop axis and the line of sight, which enters the conversion of emission measures EM(s) into electron densities $n_e(s)$. From potential field lines neighbored to the selected EUV loops we estimated also the magnetic field $B(h)$, the plasma-β parameter $\beta(h)$, and the Alfvén velocity $v_{\rm A}(h)$ along the loops. The physical parameters obtained with this stereoscopic three-dimensional method have therefore an unprecedented accuracy. The statistical results of geometric and physical parameters of the analyzed 30 EUV loops of AR 7986 are listed in Table 4.

The major findings and conclusions of this analysis are as follows:

1. The analyzed cool EUV loops are in *hydrostatic equilibrium*, i.e., the mean scale height temperature is identical to the filter-ratio temperature, $T_e^{\lambda} \approx T_e^{\rm EIT}$, and the density profile $n_e(h)$ is nearly exponential. The high accuracy of this result could only be accomplished by proper reconstruction of the three-dimensional loop geometry, in particular by the stereoscopic measurement of the inclination angle ϑ of the loop planes. The existence of hydrostatic equilibrium is physically plausible because pressure gradients can be quickly adjusted to the gravitational scale height, since the loop cooling times are found to be much longer than the sound travel time across a scale height.

2. The *loop width* $w(s)$ is found to be almost *constant* for most of the analyzed loops. Only four out 30 loops show a significant divergence with height, as is expected for dipolar fields. The constant thickness of EUV loops indicates the presence of current-induced nonpotential magnetic fields (Wang & Sakurai 1998), consistent with the findings from SXR loops (Klimchuk et al. 1992). However, we cannot make a statement about the magnitude of nonpotential fields because we measure the geometric divergence only over a segment of 1 scale height.

3. The *potential magnetic field* is found to convey an adequate representation of the coronal magnetic field traced out by EIT loops in some parts of the active region, whereas significant deviations are present in other parts. The ratio of the thermal to the magnetic pressure is found to be always $\beta \lesssim 1$ up to the apexes of the EIT loops, warranting magnetic confinement in all parts of the EUV loops. The Alfvén velocity is found to be highest near the loop footpoints and reaches asymptotically values in the range of $v_{\rm A} \approx$ 500–1000 km s^{-1} in the upper parts of the loops.

4. We find the following scaling laws between the loop length L, the loop base pressure p_0, the footpoint magnetic field $B_{\rm foot}$, and the steady state heating requirement E_{H0}: $p_0 \propto L^{-0.41\pm0.12}$, $B_{\rm foot} \propto L^{-1.02\pm0.43}$, $E_{H0} \propto L^{-0.73\pm0.23}$, $E_{H0} \propto p_0^{1.89\pm0.07}$. These scaling laws are distinctly different from steady state loop models usually applied to SXR loops, where radiative loss is comparable with conductive loss, e.g., the Rosner et al. (1978) loop scaling laws.

5. The conductive loss rate ∇F_C is found to be about 2 orders of magnitude smaller than the *radiative loss rate* E_R for these cool EUV loops, a fact that is in marked difference to hot SXR loops, where it is generally the case that $\nabla F_C \approx E_R$. The dominance of radiative cooling over conductive cooling is mainly an effect of the cooler temperature of EUV loops. As a consequence, the heating rate has to balance only the radiative loss in steady state, implying that the heating rate scales with the squared density, $E_H \propto n_e^2$, and that the heating scale height s_H corresponds to the half-density scale height λ, $s_H = \lambda/2$. However, because a steady state solution requires that radiative and conductive loss are comparable, these cool EUV loops *cannot be in steady state* equilibrium.

6. The non–steady state of cool EUV loops requires a heating function that heats uniformly or randomly along the loops because thermal conduction from a localized heating source is inefficient. This excludes heating models where the heating source is strongly localized, either at the loop top or at the footpoints. A plausible possibility is statistical heating events distributed along the entire loop that

TABLE 4

STATISTICAL RESULTS OF GEOMETRIC AND PHYSICAL PARAMETERS OF THE ANALYZED 30 EUV LOOPS OF AR 7986

Parameter	Value
Loop radius (Mm)	$R_0 = 93 \pm 23$
Offset of circular loop center from baseline (Mm)	$Z_0 = 62 \pm 27$
Loop height (Mm)	$h = 128 \pm 56$
Loop length (Mm)	$L = 433 \pm 136$
Length of traced loop segments (Mm)	$L_1 = 89 \pm 29$
Loop width (Mm)	$w = 7.1 \pm 0.8$
Loop aspect ratio	$L/w = 61 \pm 20$
Azimuth angle of loop baselines (deg)	$\alpha = 3 \pm 10$
Inclination angle of loop planes (deg)	$\vartheta = 7 \pm 37$
Base emission measure (cm^{-5})	$EM_0 = 10^{27.61 \pm 0.61}$
Base electron density (cm^{-3})	$n_{e0} = (1.92 \pm 0.56) \times 10^9$
Base pressure (dyne cm^{-2})	$p_0 = 0.61 \pm 0.17$
Density scale height (Mm)	$\lambda = 55 \pm 10$
Scale height temperature (MK)	$T_e^{\lambda} = 1.22 \pm 0.23$
EIT 171/195 Å filter-ratio temperature (MK)	$T_e^{EIT} = 1.21 \pm 0.06$
Temperature gradient (K km^{-1})	$dT/ds = 0.96 \pm 4.26$
Conductive loss rate (ergs cm^{-3} s^{-1})	$\nabla F_C = (-0.003 \pm 0.005) \times 10^{-3}$
Radiative loss rate (ergs cm^{-3} s^{-1})	$E_R = (-0.458 \pm 0.285) \times 10^{-3}$
Steady state heating rate (ergs cm^{-3} s^{-1})	$E_H = (+0.455 \pm 0.283) \times 10^{-3}$
Conductive cooling time (s)	$\tau_{cond} = 9 \times 10^5$ (10 days)
Radiative cooling time (s)	$\tau_{rad} = 2 \times 10^3$ (40 minutes)
Ratio of conductive to radiative loss time	$\tau_{cond}/\tau_{rad} = 450$
Magnetic field strength at footpoints (G)	$\lvert B_{foot} \rvert = 20, \ldots, 230$
Magnetic dipole depth (Mm)	$h_D \approx 75$
Ratio thermal/magnetic pressure at footpoints	$\beta(h = 0) = 0.001, \ldots, 0.01$
Ratio thermal/magnetic pressure at loop tops	$\beta(h = 100 \text{ Mm}) = 0.04, \ldots, 0.15$
Alfvén velocity at loop footpoints (km s^{-1})	$v_A(h = 0) = 2000, \ldots, 6000$
Alfvén velocity at loop tops (km s^{-1})	$v_A(h = 100 \text{ Mm}) = 500, \ldots, 1000$

balance the local radiative loss. The radiative cooling time increases with loop height because of the hydrostatic density structure and thus leads naturally to a positive temperature gradient along the loop. A mean recurrence time of $\lesssim 10$ minutes for individual heating events at a given location can reproduce the observed temperature gradients measured in EUV loops. Possible candidates for such a statistical heating function are nanoflares, dissipated Alfvén waves, or mass injections.

The obtained conclusions rely on the correctness of the density and temperature measurements, for which we quoted accountable uncertainties. The quoted uncertainties do not include possible systematic errors that could not be quantified in this study, such as calibration errors of the EIT instrument, uncertainties of coronal abundances used in the computation of the EIT response function, including FIP effects of some elements, or newer calculations of the radiative loss function (e.g., currently computed by J. Cook). The major progress of this study lies in a more rigorous reconstruction of the three-dimensional geometry of coronal loops (which has virtually not been attempted in earlier studies) and thus should provide more reliable values of electron densities free from projection and line-of-sight convolution effects. In future work we will analyze the hotter loops $T_e \gtrsim 1.5$ MK of this active region with stereoscopic methods. A further goal is to investigate the time variability of cool and hot active region loops, their steady state phases, and transitions to nonequilibrium states.

We thank the anonymous referee and a number of people for suggestions and helpful discussions, including John Cook, Dan Moses, Charles Kankelborg, Stephen White, Tim Bastian, Arnold Benz, and Pascal Demoulin. *SOHO* is a project of international cooperation between ESA and NASA. The work of M. J. A. was supported by NASA grants NAG-54551 and NAG-57233 through the *SOHO* Guest Investigator Program. W. M. N. was supported by NASA Contract NAS5-32350 with the Hughes STX Corporation. A. Z. was supported by a summer internship at GSFC through grant NCC5-83 with the Catholic University of America (CUA).

APPENDIX A

HELIOGRAPHIC COORDINATE SYSTEMS AND TRANSFORMATIONS

For analysis of observed images, for time-dependent coordinate transformations that take the solar rotation into account (as needed in stereoscopic correlations), and for convenient definitions of loop geometries we define three different coordinate systems:

Image coordinate system (x, y, z).—The (x, y) coordinates refer to the x-axis and y-axis of an observed image, whereas the coordinate (z) is orthogonal to the image, or parallel to the line-of-sight direction, defined positive toward the observer. The origin $(x, y, z) = (0, 0, 0)$ of this coordinate system is most conveniently assumed at the Sun center position. A solar FITS image should contain the position of the Sun center in pixel units (i_{x0}, j_{y0}) (in FITS header *CRPIX1*, *CRPIX2* or *E_XCEN*, *E_YCEN*), the pixel size $(\Delta x, \Delta y)$ in units or arcseconds (in FITS header *CDELT1*, *CDELT2*), and the solar radius i_{r0} in pixel units (in FITS header *SOLAR_R*, or *E_XSMD*, *E_YSMD* if the semidiameters of an ellipse are fitted). With this information, a pixel position (i, j) can then be converted into the coordinate system (x, y) by

$$x_i = \Delta x(i - i_{x0}) , \tag{A1}$$

$$y_i = \Delta y(j - j_{y0}) , \tag{A2}$$

where Δx = arcseconds pixel^{-1} for (x, y) in units of arcseconds, or $\Delta x = R_\odot/i_{r0}$, with $R_\odot = 696{,}000$ km, if physical length units (km) are preferred.

Heliographic coordinate system (l, b, r).—The heliographic coordinate system is corotating with the solar surface. A position on the solar surface is generally specified by heliographic longitude and latitude coordinates (l, b) (in units of heliographic degrees), with reference to the Carrington rotation grid. The heliographic longitude and latitude $[l_0(t), b_0(t)]$ of the Sun center and the position angle $P(t)$ of the solar rotation axis for a given time t are published in The Astronomical Almanac (Nautical Almanac Office, NRL, Washington DC). The two-dimensional spherical coordinate system (l, b) can be generalized into a three-dimensional coordinate system by incorporating the height h above the solar surface, which can be expressed as a dimensionless distance to the Sun center (in units of solar radii),

$$r = \left(1 + \frac{h}{R_\odot}\right) . \tag{A3}$$

The transformation from the three-dimensional heliographic coordinate system (l, b, r) into image coordinates (x, y, z) can be accomplished by applying a series of four rotations to the (normalized) vector $(0, 0, r)$ (see also Loughhead, Wang, & Blows 1983),

$$\begin{pmatrix} x/R_\odot \\ y/R_\odot \\ z/R_\odot \end{pmatrix} = \begin{pmatrix} \cos(P + P_0) & -\sin(P + P_0) & 0 \\ \sin(P + P_0) & \cos(P + P_0) & 0 \\ 0 & 0 & 1 \end{pmatrix} \begin{pmatrix} 1 & 0 & 0 \\ 0 & \cos b_0 & -\sin b_0 \\ 0 & \sin b_0 & \cos b_0 \end{pmatrix}$$

$$\begin{pmatrix} \cos(l_0 - l) & 0 & -\sin(l_0 - l) \\ 0 & 1 & 0 \\ \sin(l_0 - l) & 0 & \cos(l_0 - l) \end{pmatrix} \begin{pmatrix} 1 & 0 & 0 \\ 0 & \cos -b & -\sin -b \\ 0 & \sin -b & \cos -b \end{pmatrix} \begin{pmatrix} 0 \\ 0 \\ r \end{pmatrix} , \tag{A4}$$

where (l_0, b_0) are the heliographic longitude and latitude of the Sun center, P is the position angle of the solar rotation axis with respect to the north-south direction (defined positive toward east), and P_0 is the image rotation (roll) angle with respect to the north-south direction ($P + P_0 = 0$ for images rotated to solar north). In stereoscopic correlations, only the longitude of the Sun center, $l_0(t)$, is time-dependent in first order (according to the solar rotation rate), whereas $b_0(t)$ and $P(t)$ are slowly varying and thus almost constant for short time intervals.

Loop plane coordinate system (X, Y, Z).—To parametrize coronal loops it is also convenient to introduce a Cartesian system that is aligned with the loop footpoint baseline (X-axis) and coincides with the loop plane (X-Z plane, $Y = 0$). For instance, a circular loop model defined in the X-Z plane is specified in equations (10)–(11). The transformation of loop coordinates $(X, Y = 0, Z)$ into Cartesian coordinate system (X', Y', Z') that is aligned with the heliographic coordinate system (l, b, r) can simply be accomplished with help of two rotations,

$$\begin{pmatrix} X' \\ Y' \\ Z' \end{pmatrix} = \begin{pmatrix} \cos\alpha & -\sin\alpha & 0 \\ \sin\alpha & \cos\alpha & 0 \\ 0 & 0 & 1 \end{pmatrix} \begin{pmatrix} 1 & 0 & 0 \\ 0 & \cos\vartheta & \sin\vartheta \\ 0 & -\sin\vartheta & \cos\vartheta \end{pmatrix} \begin{pmatrix} X \\ Y \\ Z \end{pmatrix} , \tag{A5}$$

where the *azimuth angle* α denotes the angle between the loop footpoint baseline and the east-west direction and ϑ represents the inclination or tilt angle between the loop plane and the vertical to the solar surface (Fig. 2). Placing the origin of the loop coordinate system $[X = 0, Y = 0, Z = 0]$ (which is also the origin of the rotated coordinate system $[X' = 0, Y' = 0, Z' = 0]$ at heliographic position (l_1, b_1) at an altitude $h_{\rm Foot}$ above the solar surface, the transformation into heliographic coordinates is then given by

$$\begin{pmatrix} l \\ b \\ r \end{pmatrix} = \begin{pmatrix} l_1 + \arctan[X'/(Z' + h_{\rm foot} + R_\odot)] \\ b_1 + \arctan[Y'/(Z' + h_{\rm foot} + R_\odot)] \\ \sqrt{[X'^2 + Y'^2 + (Z' + h_{\rm foot} + R_\odot)^2]}/R_\odot \end{pmatrix} . \tag{A6}$$

APPENDIX B

LINE-OF-SIGHT CORRECTION ON LOOP COLUMN DEPTH

Column depth of loops with constant cross section.—In order to convert observed emission measures $\mathrm{EM}(x, y) = \int n_e^2(x, y, z)\, dz$ into local electron densities $n_e(x, y, z)$ we need information on the column depth $\int dz$. An approximation that is often useful is coronal loops with a constant cross section w, which can be measured from the FWHM as it appears perpendicular to the line of sight in the plane of the sky. For three-dimensional models of loops parametrized by coordinates (x_i, y_i, z_i), the angle ψ between the line of sight and a loop segment can then directly be derived by the ratio of the projected to the effective length of a loop segment $[i, i+1]$.

$$\cos(\psi[x_i, y_i, z_i]) = \frac{\sqrt{(x_{i+1} - x_i)^2 + (y_{i+1} - y_i)^2}}{\sqrt{(x_{i+1} - x_i)^2 + (y_{i+1} - y_i)^2 + (z_{i+1} - z_i)^2}} \tag{B1}$$

yielding the column depth w_z along the line-of-sight axis z,

$$w_z[x_i, y_i, z_i] = \frac{w}{\cos(\psi[x_i, y_i, z_i])} \quad . \tag{B2}$$

REFERENCES

Alexander, D., & Katsev, S. 1996, Sol. Phys., 167, 153
Allen, C. W. 1973, Astrophysical Quantities (London: Athlone)
Aschwanden, M. J. 1995, Lect. Notes Phys., 444, 13
Aschwanden, M. J., & Bastian, T. S. 1994a, ApJ, 426, 425
———. 1994b, ApJ, 426, 434
Aschwanden, M. J., Bastian, T. S., Nitta, N., Newmark, J., Thompson, B. J., & Harrison, R. A. 1998a, in ASP Conf. Ser. 155, Second Advances in Solar Physics Euroconference: Three-Dimensional Structure of Solar Active Regions, ed. C. Alissandrakis & B. Schmieder (San Francisco: ASP), 311
Aschwanden, M. J., Lim, J., Gary, D. E., & Klimchuk, J. A. 1995, ApJ, 454, 412
Aschwanden, M. J., et al. 1998b, in ASP Conf. Ser. 155, Second Advances in Solar Physics Euroconference: Three-Dimensional Structure of Solar Active Regions, ed. C. Alissandrakis & B. Schmieder (San Francisco: ASP), 145
Berton, R., & Sakurai, T. 1985, Sol. Phys., 96, 93
Bray, R. J., Cram, L. E., Durrant, C. J., & Loughhead, R. E. 1991, Plasma Loops in the Solar Corona (Cambridge: Cambridge Univ. Press)
Brekke, P., Kjeldseth-Moe, O., Brynildsen, N., Maltby, P., Haugan, S. V. H., Harrison, R. A., Thompson, W. T., & Pike, C. D. 1997, Sol. Phys., 170, 163
Brosius, J. W., Davila, J. M., Thomas, R. J., Saba, J. L. R., Hara, H., & Monsignori-Fossi, B. C. 1997, ApJ, 477, 969
Brosius, J. W., Willson, R. F., Holman, G. D., & Schmelz, J. T. 1992, ApJ, 386, 347
Brown, S. F. 1996, A&A, 305, 649
Cargill, P. J. 1994, ApJ, 422, 381
Cargill, P. J., & Klimchuk, J. A. 1997, ApJ, 478, 799
Cheng, C. C. 1980, ApJ, 238, 743
Davila, J. M. 1994, ApJ, 423, 871
Delaboudinière, J. P., et al. 1995, Sol. Phys., 162, 291
Dere, K. P. 1982, Sol. Phys., 75, 189
Dere, K. P., Landi, E., Mason, H. E., Monsignori-Fossi, B. F., & Young, P. R. 1997, A&AS, 125, 149
Dulk, G. A., & McLean, D. J. 1978, Sol. Phys., 57, 279
Fludra, A., Brekke, P., Harrison, R. A., Mason, H. E., Pike, C. D., Thompson, W. T., & Young, P. R. 1997, Sol. Phys., 175, 487
Foukal, P. 1975, Sol. Phys., 43, 327
———. 1978, ApJ, 223, 1046
Galeev, A. A., Rosner, R., Serio, S., & Vaiana, G. S. 1981, ApJ, 243, 301
Gary, G. A. 1990, Mem. Soc. Astron. Italiana, 61, 457
———. 1997, Sol. Phys., 174, 241
Gary, G. A., & Alexander, D. 1999, Sol. Phys., in press
Golub, L., Herant, M., Kalata, K., Lovas, I., Nystrom, G., Pardo, F., Spiller, E., & Wilczynski, J. 1990, Nature, 344, 842
Golub, L., Maxson, C., Rosner, R., Serio, S., & Vaiana, G. S. 1980, ApJ, 238, 343
Habbal, S. R., Ronan, R., & Withbroe, G. L. 1985, Sol. Phys., 98, 323
Harvey, K. L., & Hudson, H. S. 1998, in Proc. *Yohkoh* Workshop, Observational Plasma Astrophysics: Five Years of *Yohkoh* and Beyond, ed. T. Watanabe, T. Kosugi, & A. C. Sterling (Astrophys. and Space Science Library; Dordrecht: Kluwer), 229, 315
Hudson, H. S., LaBonte, B. J., Sterling, A. C., & Watanabe, T. 1998, in Proc. *Yohkoh* Workshop, Observational Plasma Astrophysics: Five Years of *Yohkoh* and Beyond, ed. T. Watanabe, T. Kosugi, & A. C. Sterling (Astrophys. and Space Science Library; Dordrecht: Kluwer), 229, 237
Kankelborg, C. C., Walker, A. B. C., II, & Hoover, R. B. 1997, ApJ, 491, 952
Kano, R., & Tsuneta, S. 1995, ApJ, 454, 934
———. 1996, Publ. Astron. Soc. Japan, 48, 535
Klimchuk, J. A., & Gary, D. E. 1995, ApJ, 448, 925
Klimchuk, J. A., Lemen, J. R., Feldman, U., Tsuneta, S., & Uchida, Y. 1992, PASJ, 44, L181
Klimchuk, J. A., & Porter, L. J. 1995, Nature, 377, 131
Lang, K. R. 1980, Astrophysical Formulae (Berlin: Springer)
Loughhead, R. E., Chen, C. L., & Wang, J. L. 1984, Sol. Phys., 92, 53
Loughhead, R. E., Wang, J. L., & Blows, G. 1983, ApJ, 274, 883
Mandrini, C. H., Demoulin, P., & Klimchuk, J. A. 1999, ApJ, submitted
Martens, P. C. H., & Kuin, N. P. M. 1982, A&A, 112, 366
McClymont, A. N., Jiao, L., & Mikić, Z. 1997, Sol. Phys., 174, 191
Meyer, J. P. 1985, APJS, 57, 173
Moses, D., et al. 1997, Sol. Phys., 175, 571
Neupert, W. M., et al. 1998, Sol. Phys., 183, 305
Newmark, J. S., Delaboudinière, J. P., Dere, K. P., Gurman, J. B., Lemen, J. R., & Thompson, B. J. 1996, EOS, Vol. 77, 46, 557
Newmark, J. S., Thompson, B., Gurman, J. B., Delaboudinière, J. P., Aschwanden, M. J., & Mason, H. 1997, BAAS, 29/5, 1321, 73.07
Nitta, N., et al. 1991, ApJ, 374, 374
Ofman, L., Klimchuk, J. A., & Davila, J. M. 1998, ApJ, 493, 474
Pallavicini, R., Serio, S., & Vaiana, G. S. 1977, ApJ, 216, 108
Parker, E. N. 1988, ApJ, 330, 474
Peres, G. 1997, in Proc. 5th *SOHO* Workshop on The Corona and Solar Wind Near Minimum Activity (Nordwiijk: ESA SP-404), 55
Porter, L. J., & Klimchuk, J. A. 1995, ApJ, 454, 499
Priest, E. R. 1981, Solar Flare Magnetohydrodynamics (New York: Gordon & Breach)
Priest, E. R., Foley, C. R., Heyvaerts, J., Arber, T. D., Culhane, J. L., & Acton, L. W. 1998, Nature, 393, 545
Raymond, J. C., Cox, D. P., & Smith, B. W. 1976, ApJ, 204, 290
Rosner, R., Tucker, W. H., & Vaiana, G. S. 1978, ApJ, 220, 643
Sakurai, T. 1982, Sol. Phys., 76, 301
———. 1989, Space Sci. Rev., 51, 11
Schmelz, J. T., Holman, G. D, Brosius, J. W., & Gonzalez, R. D. 1992, ApJ, 399, 733
Schmelz, J. T., Holman, G. D., Brosius, J. W., & Willson, R. F. 1994, ApJ, 434, 786
Serio, S., Peres, G., Vaiana, G. S., Golub, L., & Rosner, R. 1981, ApJ, 243, 288
Sheeley, N. 1980, Sol. Phys., 66, 79
SOHO EIT User's Guide. 1998, http://umbra.nascom.nasa.gov/eit/eit_guide/guide.html
Spitzer, L. 1962, Physics of Fully Ionized Gases (New York: Interscience)
Vesecky, J. F., Antiochos, S. K., & Underwood, J. H. 1979, ApJ, 233, 987
Vourlidas, A., & Bastian, T. S. 1996, ApJ, 466, 1039
Wang, H., & Sakurai, T. 1998, PASJ, 50, 111
Wang, Y. M., et al. 1997, ApJ, 485, 419
Webb, D. F., Holman, G. D., Davis, J. M., Kundu, M. R., & Shevgaonkar, R. K. 1987, ApJ, 315, 716
Wheatland, M. S., Sturrock, P. A., & Acton, L. W. 1997, ApJ, 482, 510
Wragg, M. A., & Priest, E. R. 1982, A&A, 113, 269
Zhang, J., White, S. M., & Kundu, M. R. 1998, ApJ, 504, L127